

Measurement of Snowpack Density, Grain Size, and Black Carbon Concentration Using Time-domain Diffuse Optics

Connor A. HENLEY,^{1,2} Colin R. MEYER,³ Jacob I. CHALIF,⁴ Joseph L. HOLLMANN,² and Ramesh RASKAR¹

¹*MIT Media Lab, Massachusetts Institute of Technology, Cambridge, MA, USA*

²*The Charles Stark Draper Laboratory, Inc., Cambridge, MA, USA*

³*Thayer School of Engineering, Dartmouth College, Hanover, NH, USA*

⁴*Department of Earth Sciences, Dartmouth College, Hanover, NH, USA*

Correspondence: Connor Henley <chenley390@gmail.com>

ABSTRACT. Diffuse optical spectroscopy (DOS) techniques characterize scattering media by examining their optical response to laser illumination. Time-domain DOS methods involve illuminating the medium with a laser pulse and using a fast photodetector to measure the time-dependent intensity of light that exits the medium after multiple scattering events. While DOS research traditionally focused on characterizing biological tissues, we demonstrate that time-domain diffuse optical measurements can also be used to characterize snow. We introduce a model that predicts the time-dependent reflectance of a dry snowpack as a function of its density, grain size, and black carbon content. We develop an algorithm that retrieves these properties from measurements at two wavelengths. To validate our approach, we assembled a two-wavelength lidar system to measure the time-dependent reflectance of snow samples with varying properties. Rather than measuring direct surface returns, our system captures photons that enter and exit the snow at different points, separated by a small distance (4-10cm). We observe clear, linear correlations between our retrievals of density and black carbon concentration, and ground truth. For black carbon concentration the correlation is nearly one-to-one. We also find that our method is capable of distinguishing between small and large grain sizes.

INTRODUCTION

Snow is composed of transparent ice grains that absorb light very weakly at visible wavelengths (Warren, 2019). Because of this, photons that enter a snowpack will typically scatter many times off of a large number of ice grains before they either exit the medium or get absorbed. The study of snow optics has historically focused on the interaction of snow with *sunlight*, as understanding this interaction is essential to understanding snow cover's contribution to the Earth's climate (Henderson and others, 2018) and for

This is an Open Access article, distributed under the terms of the Creative Commons Attribution-NonCommercial-NoDerivatives licence (<http://creativecommons.org/licenses/by-nc-nd/4.0/>), which permits non-commercial re-use, distribution, and reproduction in any medium, provided the original work is unaltered and is properly cited. The written permission of Cambridge University Press must be obtained for commercial re-use or in order to create a derivative work.

35 forecasting snow melt (Painter and others, 2010), among other things. A key goal of snow optics has been
36 to predict spectral albedo as a function of snowpack properties—such as grain size, which determines the
37 probability that a photon will be absorbed at each scattering event (Wiscombe and Warren, 1980a), and
38 the concentration of light absorbing particles such as dust, black carbon, or algae that are mixed into the
39 snow (Wiscombe and Warren, 1980b; Skiles and others, 2018).

40 The development of accurate spectral albedo models has, in turn, led to the development of optical
41 sensing methods that retrieve grain size (Nolin and Dozier, 2000; Gallet and others, 2009) and LAP
42 concentrations (Zege and others, 2011; Painter and others, 2012) from spectral albedo measurements. These
43 methods, while useful, have limitations. Snowpack albedo is largely independent of important properties
44 such as snow density (Wiscombe and Warren, 1980a). Furthermore, spectral albedo measurements usually
45 require passive illumination by sunlight, and as such cannot be used to retrieve snow properties at night
46 and for several months of the year in polar regions. Albedo models developed for solar illumination assume
47 steady-state illumination that is collimated, diffuse, or a mixture of the two. As such, they cannot fully
48 model lidar waveform measurements, which consist of the time-dependent optical response of snowpack to
49 focused, pulsed illumination.

50 Over the past few decades, in parallel with advances in snow optics, the biomedical optics community
51 has developed a suite of techniques for characterizing biological tissue, which, like snow, is also a highly
52 scattering medium. Collectively, these methods are referred to under the umbrella term of *diffuse optical*
53 *spectroscopy* (DOS) (Durduran and others, 2010), which refers to the fact that the propagation of photons
54 within the scattering medium is modeled using the *diffusion approximation* to the radiative transfer equa-
55 tion (Welch and van Gemert, 1995), and to the fact that multi-wavelength illumination is frequently used
56 (although this is not required). In DOS techniques the tissue is probed with a focused laser source that
57 can be time-modulated, frequency-modulated, or continuous-wave. Measurements of the tissue's optical
58 response are then used to estimate its optical properties, such as the tissue's absorption coefficient or effec-
59 tive scattering coefficient. These optical properties, in turn, can be related to clinically useful properties
60 of the tissue such as blood oxygenation (Sevick and others, 1991), organelle size (Li and others, 2008), and
61 the concentrations of water, lipids, and collagen (Quarto and others, 2014). DOS has also been applied in
62 non-clinical settings for the inspection of produce (Nicolai and others, 2014), and for characterizing porous
63 materials such as wood (Bargigia and others, 2013) and pharmaceutical tablets (Johansson and others,
64 2002).

65 Because snow is also a highly scattering medium, many of the results from diffuse optical spectroscopy
66 can be adapted to the characterization of snowpack properties. Despite this, the adoption of diffuse optics
67 concepts in the snow sensing community has been limited. Várnai and Cahalan (2007) proposed that
68 the spatial spread of diffused laser light could be used to determine snow and sea ice thickness. Smith
69 and others (2018) noted that the multiple scattering of green laser light within a snowpack should result
70 in biases in lidar altimetry measurements. They used a combination of diffusion theory and Monte-carlo
71 modeling to assess the dependence of this multiple scattering bias on grain size, black carbon concentration,
72 and the choice of surface height retrieval algorithm. Smith and others (2023) used the model of Smith and
73 others (2018) to develop an algorithm that infers snow grain size from full waveform lidar measurements
74 collected by the Airborne Topographic Mapper (ATM). Fair and others (2024) use lidar retrievals of grain

75 size to predict biases in snow surface heights retrieved using green (532 nm) lidar beams on IceSat-2 and
76 ATM. As far as we are aware, prior to this work, the only direct application of DOS techniques to retrieve
77 bulk snowpack properties was made by Allgaier and Smith (2022). In their work, the snow was illuminated
78 with continuous-wave laser sources at two different wavelengths, and a smartphone camera was used to
79 take images of the spatially resolved, steady-state intensity of light that exited the snowpack after diffusing
80 within the snow. From these smartphone images, along with an independent *in situ* measurement of the
81 snow's density, the authors were able to retrieve the absorption and effective scattering coefficients of the
82 snowpack, as well as an estimate of the concentration of black carbon within it. In Ackermann and others
83 (2006), and in a separate work by Allgaier and others (2022), time-domain diffuse optical measurements
84 were used to estimate the absorption and scattering coefficients of *glacier ice*, which is optically similar to
85 snow. A theoretical analysis of diffuse optical spectroscopy applied to glacier ice is provided in Allgaier and
86 Smith (2021). Studinger and others (2024) use multiple scattering returns in green lidar measurements to
87 infer the scattering length within *sea ice*.

88 In this work we introduce a new method for characterizing the bulk properties of *snow* that is based on
89 *time-domain* diffuse optical measurements. Our instrument is effectively a photon-counting lidar system
90 that consists of two pulsed lasers with different wavelengths (one red, one near-infrared), and a single-
91 photon avalanche diode (SPAD) receiver. Rather than measuring surface returns, which might be used for
92 altimetry, we measure photons that enter the snowpack at a single point on the surface and exit at a second
93 surface point that is displaced from the point of entry by a small distance (4-10 cm). Through a series of
94 proof-of-principle experiments, we show that our method is capable of retrieving the density (through the
95 ice volume fraction), grain size, and the concentration of light absorbing particles of a dry snowpack, in a
96 non-invasive way.

97 METHODS

98 Diffusion Model

99 The propagation of a laser pulse inside a scattering medium is described by the time-dependent radiative
100 transfer equation (Welch and van Gemert, 1995), which models the flow of *radiance* ($\text{W m}^{-2} \text{sr}^{-1}$) within
101 a medium as a function of space and time. The scattering medium is described by a scattering coefficient
102 μ_s (m^{-1}), a scattering phase function, an absorption coefficient μ_a (m^{-1}), and the speed of light within the
103 medium c_* (m s^{-1}).

104 Under the *diffusion approximation* to the radiative transfer equation, photons are modeled as particles
105 that “diffuse” through a scattering medium via random walks. This approximation accurately describes
106 situations for which the distance scales considered are much larger than the mean free path of photons
107 within the medium ($= (\mu_a + \mu_s)^{-1}$), and photons are typically scattered many times before they are
108 absorbed ($\mu_s \gg \mu_a$) (Welch and van Gemert, 1995). The photon diffusion equation can be written as
109 follows:

$$\frac{1}{c_*} \frac{\partial}{\partial t} \phi(\mathbf{r}, t) - D \nabla^2 \phi(\mathbf{r}, t) + \mu_a \phi(\mathbf{r}, t) = S(\mathbf{r}, t). \quad (1)$$

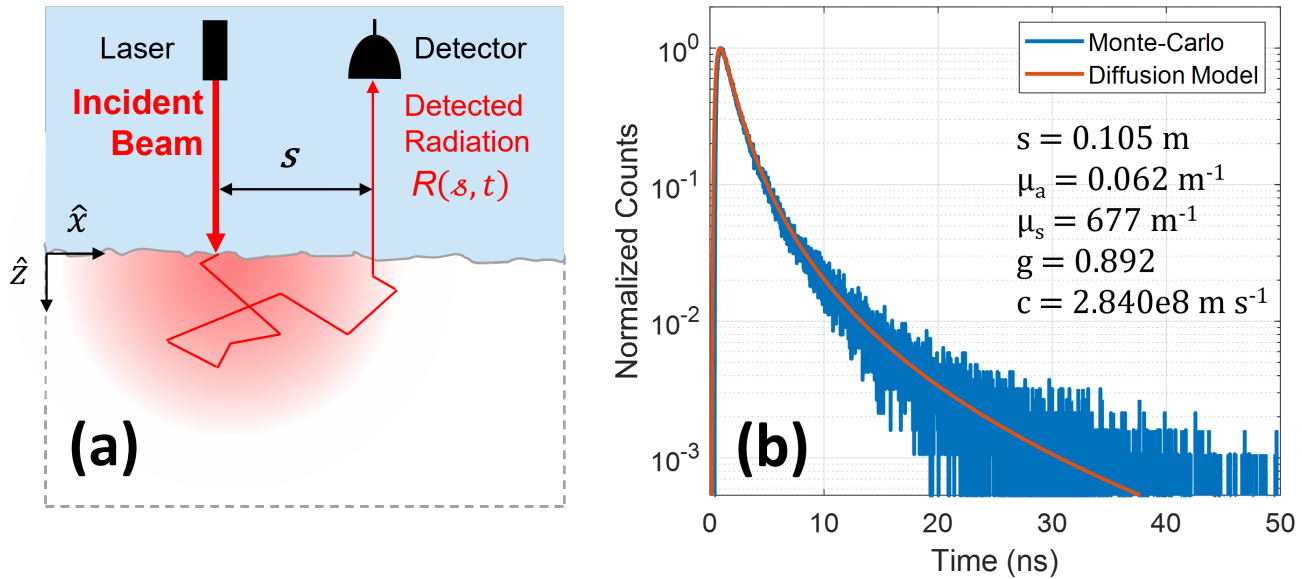


Fig. 1. (a) Illustration of the measurement geometry employed in this work. A point on the snow surface is illuminated by a laser pulse at time $t = 0$. A detector observes the time-dependent intensity of light that exits the snow from a second point at distance s from the laser spot. (b) Comparison of time-dependent intensity predicted by our model (Eq. 5), to photon time-of-flight measurements generated using a Monte-carlo simulation of a scattering medium with the same properties. Both curves are normalized to their respective peaks.

110 A derivation of the photon diffusion equation can be found in Haskell and others (1994). Unlike the
 111 time-dependent radiative transfer equation, which models the time-evolution of a five-dimensional radiance
 112 field, the photon diffusion equation models the lower dimensional quantity of *photon fluence* $\phi(\mathbf{r}, t)$ (W m^{-2}),
 113 which is the integral of radiance over all directions. The variable S represents an isotropic source term,
 114 and the diffusion constant D is defined as

$$D = \frac{1}{3[\mu_a + (1 - g)\mu_s]}. \tag{2}$$

115 Here g is the asymmetry factor of the scattering phase function, which can take values between -1
 116 and 1 depending on whether the medium is primarily backward scattering ($g < 0$), isotropically scattering
 117 ($g = 0$), or forward scattering ($g > 0$).

118 Crucially, the photon diffusion equation permits analytical solutions when the geometry of the scattering
 119 medium is sufficiently simple. We consider the scenario depicted in Fig. 1(a). Here, the medium is assumed
 120 to be semi-infinite and homogeneous. The medium's surface is illuminated by a pulsed, pencil-beam source
 121 at time $t = 0$, and a detector observes the time-dependent intensity of light that exits the medium at
 122 a second point that is displaced from the point of illumination by a distance s . Kienle and Patterson
 123 (1997) showed that, in this scenario, Eq. 1 can be accurately solved by imposing an *extrapolated boundary*
 124 *condition*, which requires that photon fluence goes to zero along a planar boundary that lies just above
 125 the medium's surface. The source term S is approximated by a point source buried one transport mean
 126 free path beneath the surface, and the equation is then solved via the method of images. This yields the
 127 following expression for photon fluence inside the medium:

$$\phi(s, z, t) = \frac{c_*}{(4\pi Dc_*t)^{3/2}} \exp(-\mu_a c_*t) \times \left\{ \exp\left[-\frac{(z - z_0)^2 + s^2}{4Dc_*t}\right] - \exp\left[-\frac{(z + z_0 + 2z_b)^2 + s^2}{4Dc_*t}\right] \right\}. \quad (3)$$

128 Here z denotes the distance from the surface, going down; $z_0 = [\mu_a + (1 - g)\mu_s]^{-1}$ is the depth of the
 129 buried point source; and z_b denotes the height of the extrapolated boundary. Haskell and others (1994)
 130 proposed a value of $z_b = \frac{1+R_{eff}}{1-R_{eff}}2D$, where R_{eff} is the fraction of photons that are internally reflected at
 131 the interface between the scattering medium and the external (non-scattering) medium due to a refractive
 132 index mismatch. Because our ultimate goal is to model the optical response of a snowpack, and because
 133 the snow-air boundary of a typical snowpack is not a dielectric interface at optical wavelengths, we assume
 134 for this work that $R_{eff} = 0$ and hence, $z_b = 2D$.

135 From Eq. 3, we compute the time dependent radiosity (W m^{-2}) that exits the surface at position s
 136 using Fick's Law (Kienle and Patterson, 1997):

$$J(s, t) = -D\nabla\phi(s, z, t) \cdot (-\hat{z})|_{z=0}. \quad (4)$$

137 The reflected flux R measured by a detector that observes the medium's surface from a distance can
 138 then be described using the following expression:

$$R(s, t) = \frac{\alpha c_*}{3(2\pi)^{3/2}} \frac{z_0^2}{(2Dc_*t)^{5/2}} \exp\left(-\mu_a c_*t - \frac{s^2 + z_0^2}{4Dc_*t}\right) \times \left[1 + \frac{7}{3} \exp\left(-\frac{10z_0^2}{9Dc_*t}\right)\right], \quad (5)$$

139 where α is a constant that encapsulates instrumental parameters such as transmitted laser power, detection
 140 efficiency, and the detector's etendue. We note that we have made liberal use of the substitutions $D = z_0/3$
 141 and $z_b = 2z_0/3$. In deriving Eq. 5, we also assumed that the surface could be accurately described
 142 as a Lambertian emitter, which means that the radiance emitted by the surface is independent of the
 143 emission angle. Previous work has relaxed this assumption (Kienle and Patterson, 1997). We found that
 144 doing so produced nearly identical results when describing a nadir-pointing detector, but added significant
 145 complexity to the model. For this reason, we elected to use Eq. 5.

146 In Fig. 1(b) we compare the time-dependent intensity predicted by Eq. 5 to simulated photon time-of-
 147 flight measurements generated using a Monte-carlo simulation (Henley, 2020). The modeled results match
 148 the simulation very closely. In general, models derived from the diffusion approximation to the radiative
 149 transfer equation accurately describe the measurements of photons that arrive at later times ($c_*t \gg z_0$) and
 150 larger distances from the laser spot ($s \gg z_0$), as these photons have scattered many times before exiting
 151 the medium.

152 Snow Scattering Model

153 Our measurement model, defined in Eq. 5, is expressed in terms of three phenomenological parameters—
 154 the absorption coefficient μ_a , the effective scattering coefficient $\mu'_s = (1 - g)\mu_s$, and the effective speed of
 155 light in the medium c_* . We use a scattering model derived from the geometric-optics scattering model of
 156 Kokhanovsky and Zege (2004) to define μ_a , μ'_s , and c_* in terms of three physically meaningful snowpack
 157 parameters— v_* , the fraction of the snowpack volume that is occupied by ice; r_* (m), the grain radius; and
 158 C_{bc} (kg kg^{-1}), the mass mixing ratio of black carbon in the snowpack. We note that, for a dry snowpack,
 159 the ice volume fraction v_* is readily converted to bulk snowpack density ρ_* (kg m^{-3}) via the expression
 160 $\rho_* = v_*\rho_{ice} + (1 - v_*)\rho_{air} \approx v_*\rho_{ice}$, where ρ_{ice} and ρ_{air} are the intrinsic densities of ice and air, respectively.
 161 We do not consider wet snow in this work.

162 Clean Snowpack

163 For a dry snowpack that contains optically insignificant concentrations of light absorbing particles, the
 164 scattering and absorption coefficients can be written entirely as functions of v_* and r_* . The absorption and
 165 effective scattering coefficients are computed as follows:

$$\mu_a = B\Gamma v_* \quad (6)$$

$$\mu'_s = \frac{3}{2}(1 - g)\frac{v_*}{r_*}, \quad (7)$$

166 The grain radius r_* can be interpreted as the characteristic size of the ice grains. As in Kokhanovsky
 167 and Zege (2004), r_* is defined as the radius of the spherical ice grain that would have the same surface-
 168 area-to-volume ratio as the ice-air matrix that comprises the true snowpack. Explicitly $r_* = 3\frac{\langle V \rangle}{\langle \Sigma \rangle}$, where
 169 $\langle V \rangle$ is the mean ice grain volume and $\langle \Sigma \rangle$ is the mean ice grain surface area.

170 The absorption enhancement parameter B and scattering asymmetry factor g are determined by grain
 171 shape (Libois and others, 2013). A recent study by Robledano and others (2023) suggests that these
 172 parameters cluster around $B = 1.7$ and $g = 0.825$ for most real snow samples, so we use those values
 173 here. These values are approximately valid for visible and near-infrared wavelengths (400nm to 14000nm)
 174 (Robledano and others, 2023). Notably, the values determined by Robledano and others (2023) closely
 175 match theoretical predictions for a two-phase random mixture of ice and air, in which grains have random
 176 and irregular shapes rather than idealized shapes such as spheres or hexagonal plates (Malinka, 2014).

177 In Fig. 2(a) we visualize the range of values for μ'_s obtained across a domain of feasible grain sizes
 178 and ice volume fractions. Figure 2(b) shows the dependence of μ_a on ice volume fraction and wavelength.
 179 Unlike μ'_s , the absorption coefficient depends strongly on wavelength, and varies by more than an order of
 180 magnitude between the red ($\lambda = 640$ nm) and near infrared ($\lambda = 905$ nm) wavelengths used in this study.

181 Effective Speed of Light in Snow

182 The last parameter to calculate is the effective speed of light within the snowpack c_* . In many problems
 183 that involve light propagation in a scattering medium, light's speed is treated as a constant that can be

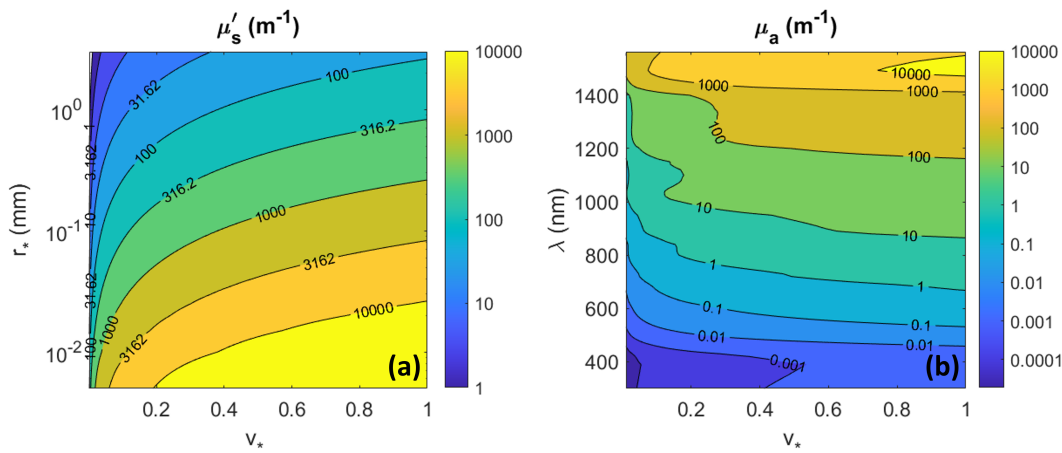


Fig. 2. (a) Effective scattering coefficient μ'_s (m⁻¹) as a function of ice volume fraction v_* (unitless) and grain radius r_* (mm). (b) Absorption coefficient μ_a (m⁻¹) of clean snow as a function of ice volume fraction v_* (unitless) and wavelength λ (nm).

184 computed beforehand if the medium’s index of refraction is known. This approach does not work for snow,
 185 which is a heterogeneous mixture of two materials—ice and air—that have markedly different refractive
 186 indices and that may be mixed at any ratio.

187 The geometric scattering model proposed by Kokhanovsky and Zege (2004), from which we defined
 188 μ_a and μ'_s (Eqs. 6, 7), implicitly defines the distance that a photon travels through an ice grain as the
 189 distance (i.e. l_{ice}) of the chord that connects the points at which a photon enters (point 1 in Fig. 3) and
 190 exits (point 3) the grain. This effective “transportation distance” differs from the *true* distance (i.e. l'_{ice})
 191 traveled through the grain if the photon is internally reflected (e.g. at point 2) before it exits the grain. The
 192 absorption enhancement parameter B is approximately equal to the ratio between the true and effective
 193 transportation distances, averaged over all possible internal paths (i.e. $l'_{ice} \approx Bl_{ice}$) (Libois and others,
 194 2019).

195 An effective light speed model that is compatible with our definitions of μ_a and μ'_s must describe the
 196 average speed at which light advances along this effective transportation path, which is equivalent to the
 197 true photon path in the air phase, but shorter than the true photon path in the ice phase by a factor of
 198 B . If a photon travels along an effective transportation path of length L , on average that path will pass
 199 through $(1 - v_*)L$ of air and v_*L of ice. The time T require to traverse this path is

$$T = \frac{(1 - v_*)L}{c_0} + \frac{n_{ice}Bv_*L}{c_0}, \tag{8}$$

200 where n_{ice} is the real component of the refractive index of ice (Warren and Brandt, 2008) and c_0 is the
 201 speed of light in air (where it’s assumed that $n_{air} = 1$). The travel time within the ice phase has been
 202 increased by a factor B to account for the difference between the true and effective transportation path
 203 lengths. Dividing L by T leaves us with

$$c_* = \frac{c_0}{1 + (n_{ice}B - 1)v_*}. \tag{9}$$

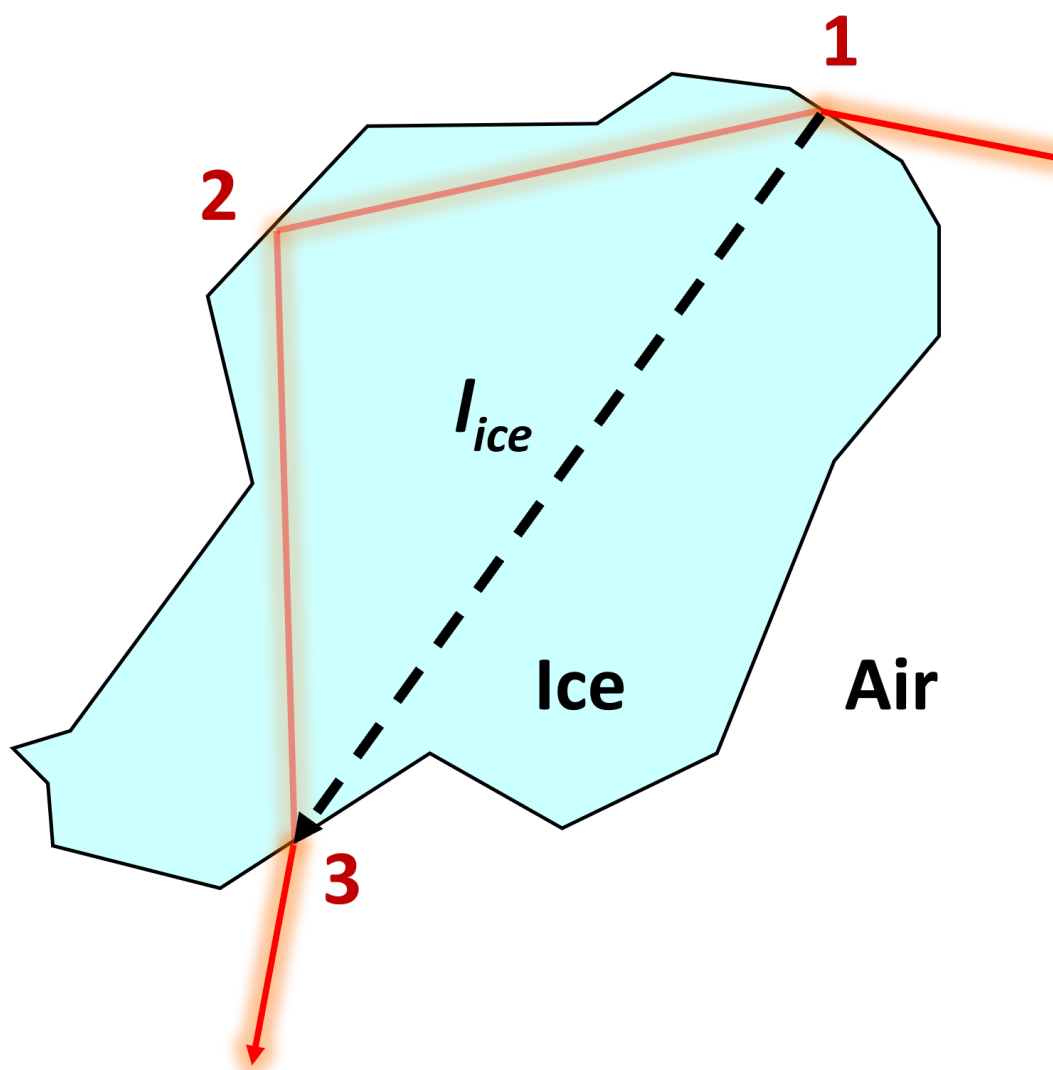


Fig. 3. A comparison of the true path (red) traveled by a photon through an ice grain, including internal reflections, to the effective transportation path (black, dashed) of length l_{ice} that is implicitly assumed by our absorption and effective scattering coefficient models.

204 We stress that the effective light speed defined here is *lower* than the mean speed of light computed with
 205 respect to the lengths of true photon paths through snow, which due to internal reflections can include
 206 jagged paths within grains. An expression for this true mean light speed was computed by Libois and
 207 others (2019), and is equal to the effective light speed of Eq. 9, multiplied by a factor of $[1 + (B - 1)v_*]$.

208 *Effect of Light Absorbing Impurities*

209 Ice is an exceptionally weak absorber of light at visible wavelengths (Warren, 2019). As such, the absorption
 210 of visible light within a snowpack can be enhanced significantly—even dominated—by the presence of trace
 211 concentrations of more absorptive substances. This has the important effect of reducing snowpack albedo,
 212 which increases radiative forcing on the snow surface and subsequently enhances snow melt and metamor-
 213 phism and can also influence the local climate (Skiles and others, 2018). For our purposes, the presence
 214 of small concentrations of LAPs can increase the absorption coefficient of a snowpack considerably—thus
 215 rendering Eq. 6, our model for clean snowpack absorption, insufficient. Globally, radiative forcing from
 216 LAPs is dominated by black carbon, mineral dust, organic or “brown” carbon, and snow algae (Skiles and
 217 others, 2018). Here we assume that absorption by LAPs is dominated by black carbon, but note that our
 218 model could be extended to include other types of particles by modifying the LAP absorption spectrum
 219 used here.

220 According to Flanner and others (2012), between 32-73% of the black carbon in global surface snow
 221 is embedded within ice grains (or “internally mixed”), with the remainder being external to those grains
 222 (“externally mixed”) in the air phase. The elongated paths followed by photons within ice increases the
 223 probability that photons will interact with internally mixed black carbon particles. As a consequence, in-
 224 ternally mixed black carbon has an outsized impact on snow absorption and albedo, relative to externally
 225 mixed black carbon (Flanner and others, 2012). Models for snow’s absorption coefficient that consider the
 226 mixing state of black carbon have been proposed (Liou and others, 2014; Dombrovsky and Kokhanovsky,
 227 2020), however these models typically require idealized grain shapes such as spheres—which do not accu-
 228 rately represent real snow—and assign highly non-linear dependencies on black carbon concentration that
 229 are grounded in electromagnetic theory (Dombrovsky and Kokhanovsky, 2020) or stochastic simulations
 230 (Liou and others, 2014).

231 Here we propose a simple geometric optics model for the additional absorption due to black carbon
 232 that can be computed from the bulk density of black carbon particles embedded inside ice grains ρ_{bc}^{in} (kg
 233 m^{-3}), the bulk density of black carbon particles external to the grains ρ_{bc}^{out} (kg m^{-3}), and the wavelength-
 234 dependent mass absorption efficiency MAE_{bc} ($m^2 \text{ kg}^{-1}$) of the black carbon particles (Grenfell and others,
 235 2011). Under this model, the presence of black carbon in a snowpack alters its properties primarily by
 236 adding an extra term to the absorption coefficient, i.e. $\mu_a^{snow} = \mu_a^{ice} + \mu_a^{bc}$. Our proposed model is written
 237 as follows:

$$\begin{aligned} \mu_a^{bc} &= MAE_{bc} \left[(1 - v_*) \rho_{bc}^{out} + B v_* \rho_{bc}^{in} \right] \\ &= MAE_{bc} \rho_{ice} v_* \left[(1 - v_*) C_{bc}^{out} + B v_* C_{bc}^{in} \right]. \end{aligned} \quad (10)$$

238 Here absorption by internally mixed impurities is multiplied by the absorption enhancement factor B

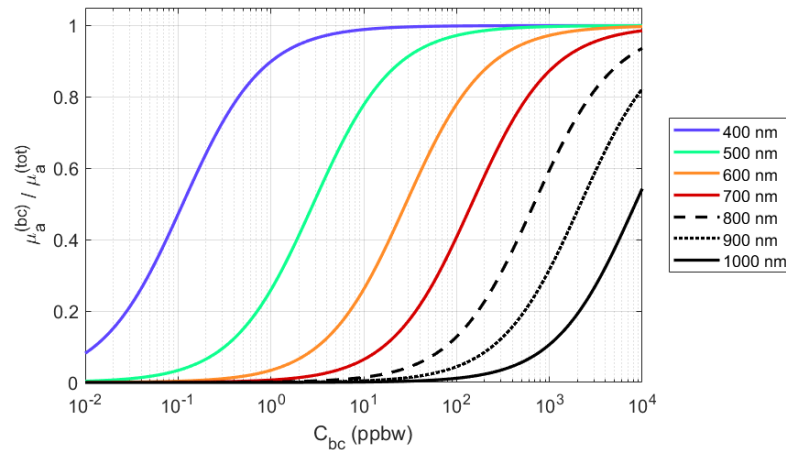


Fig. 4. The ratio of light absorption due to black carbon to total absorption by the snowpack for a range of wavelengths. Ratio computation assumes ice volume fraction $v_* = 0.3$.

239 to account for the elongation of photon paths within ice grains. In the lower part of Eq. 10, we replace ρ_{bc}^{in}
 240 and ρ_{bc}^{out} with the products of the intrinsic density of ice ($\rho_{ice} = 916.5 \text{ kg m}^{-3}$), the snowpack’s ice volume
 241 fraction v_* , and the mass mixing ratios C_{bc}^{in} and C_{bc}^{out} of internally and externally mixed black carbon,
 242 respectively.

243 To simplify our model further, we assume that the black carbon is evenly mixed, i.e. $C_{bc}^{in} = C_{bc}^{out}$. We
 244 then combine Eqs. 6 and 10 to obtain a complete expression for the snowpack absorption coefficient:

$$\mu_a = B\Gamma v_* + MAE_{bc} \rho_{ice} C_{bc} v_* [1 + (B - 1)v_*]. \tag{11}$$

245 Following the example of Doherty and others (2014), we model the wavelength dependence of MAE_{bc}
 246 using a power law spectrum:

$$MAE_{bc}(\lambda) = MAE_{bc}(\lambda_{ref}) (\lambda_{ref}/\lambda)^{\mathring{A}}, \tag{12}$$

247 that has an Ångstrom coefficient $\mathring{A} = 1.1$ and is referenced to $MAE_{bc}(\lambda_{ref}) = 6500 \text{ m}^2 \text{ kg}^{-1}$, where
 248 $\lambda_{ref} = 600 \text{ nm}$.

249 Fig. 4 illustrates that, for a fixed C_{bc} , the fraction of absorption attributable to black carbon in snow
 250 depends strongly on the wavelength of light that interacts with the snowpack. We plot the ratio of
 251 absorption due to black carbon (using Eq. 10) to the total absorption (from Eq. 11) for a selection of
 252 wavelengths that range from 400 nm (blue) to 1000 nm (near infrared). In computing these ratios, we
 253 assume an ice volume fraction of $v_* = 0.3$. For blue light, our model suggests that absorption is entirely
 254 dominated by just 1 part per billion by weight (ppbw) of black carbon, which is comparable to mass mixing
 255 ratios found in Greenlandic snow (Warren, 2019). In contrast, at 1000 nm, absorption from black carbon
 256 only eclipses ice absorption for mass mixing ratios above 7500 ppbw—a very high level of soot that would
 257 cause the snow to appear visibly grey. This decreased sensitivity at longer wavelengths is not caused by
 258 the decreased absorption of black carbon at these wavelengths, but rather by the increased absorption
 259 efficiency of ice.

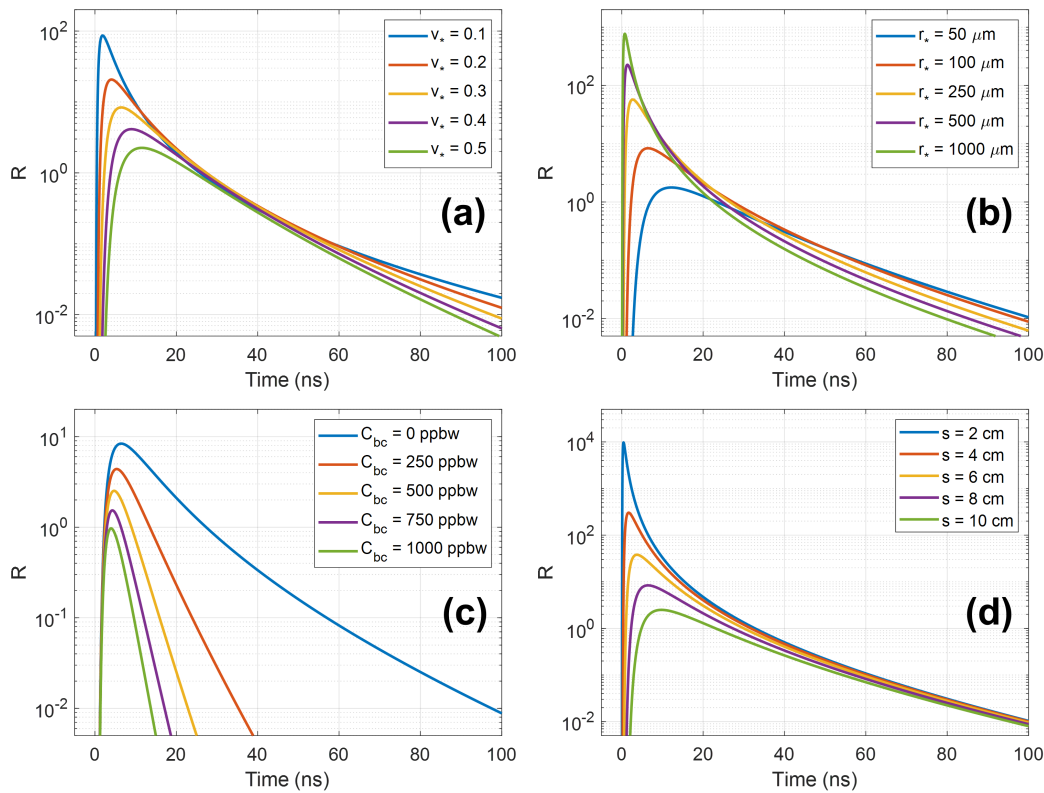


Fig. 5. Plots of predicted time-dependent flux measured by a detector observing snow following illumination by a laser pulse ($\lambda = 640$ nm). Curves were produced using Eq. 5 and μ_a , μ'_s , and c_* were computed from v_* , r_* , and C_{bc} using Eqs. 11, 7, and 9, respectively. (a) Ice volume fraction v_* is varied. $r_* = 100 \mu\text{m}$, $C_{bc} = 0$ ppbw, and $s = 8$ cm. (b) Grain radius r_* is varied. $v_* = 0.3$, $C_{bc} = 0$ ppbw, and $s = 8$ cm. (c) Impurity concentration C_{bc} is varied. $v_* = 0.3$, $r_* = 100 \mu\text{m}$, and $s = 8$ cm. (d) Detector focus position s is varied. $v_* = 0.3$, $r_* = 100 \mu\text{m}$, and $C_{bc} = 0$ ppbw.

260 *Effect of Snow Properties on Time-domain Response*

261 Having obtained expressions that relate μ_a , μ'_s , and c_* to the grain size, ice volume fraction, and black
 262 carbon concentration of a dry snowpack, we can now develop an understanding of how changes to v_* , r_* ,
 263 and C_{bc} affect the snowpack's time-domain optical response. Upon inspection of Eq. 5, we see that the
 264 shape of a snowpack's transient response is primarily controlled by $\mu_a c_*$, which determines the rate of
 265 decay of the signal's tail; $2Dc_*$, which can be interpreted as the rate at which a Gaussian cloud of diffusing
 266 photons expands over time, and which controls the position of the signal's peak; and z_0^2 , which influences
 267 the shape of the response at the earliest arrival times, but in practice has little effect when $s \gg z_0$.

268 The exponential decay rate, $\mu_a c_*$, depends on v_* and C_{bc} . On the other hand, $2Dc_*$ and z_0^2 primarily
 269 depend on the medium's scattering coefficient, which in turn depends on the ratio v_*/r_* . These effects are
 270 visualized in Figs 5(a), (b), and (c), where we plot the predicted transient response curves for snowpack
 271 with varying v_* , r_* , and C_{bc} . For these curves, the snow is probed with red (640 nm) light, and the position
 272 of the detector's focus spot is fixed at $s = 8$ cm.

273 In Fig. 5(a) we see that for a clean snowpack ($C_{bc} = 0$), as v_* is increased while r_* is held constant, the
 274 slope of the signals' exponential tail becomes more steep as light is absorbed by the medium more quickly.
 275 The arrival time of the signal peak is also pushed back because tighter packing of the ice grains reduces

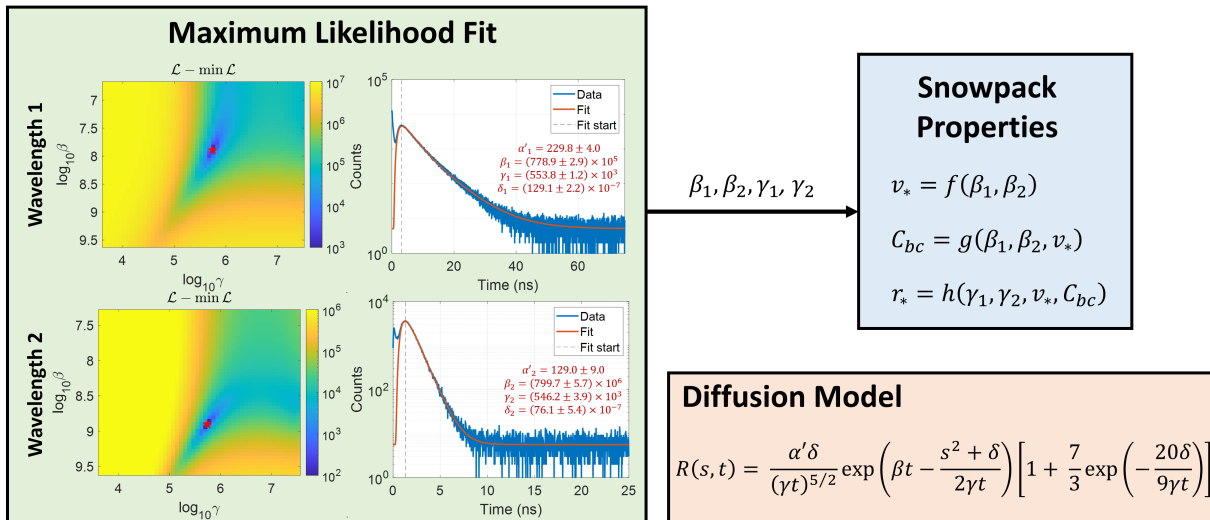


Fig. 6. (Left) A diffusion model (lower right) is fit to photon time-of-flight histograms measured at two wavelengths. Fit parameters α' , β , γ , and δ are determined using a grid search algorithm that minimizes a negative Poisson log-likelihood function. (Top right) Snowpack properties v_* , r_* , and C_{bc} are computed directly from parameters β_1 , β_2 , γ_1 , and γ_2 by evaluating analytical expressions (Eqs. 17, 18, and 19)

276 the distance between photon scattering events, thus reducing the rate at which light diffuses within the
 277 medium.

278 In Fig. 5(b), r_* is varied while v_* is held constant and again $C_{bc} = 0$. As grain size increases, grains
 279 must be spaced further apart to maintain the same density, thus increasing the rate of diffusion within the
 280 medium. As such, for a fixed snow density and source-detector separation, the peak of the diffusion signal
 281 will arrive earlier, and will be more intense, when the grains are large.

282 In Fig. 5(c), v_* and r_* are held fixed while C_{bc} is varied. Black carbon content only influences the
 283 absorption coefficient of the snowpack, and so increasing C_{bc} steepens the exponential decay rate $\mu_a C_*$. At
 284 the probing wavelength of 640 nm (where ice is a relatively weak absorber) the influence of C_{bc} is quite
 285 dramatic when compared to the comparable influence of ice volume fraction on the exponential decay rate,
 286 shown in Fig. 5(a).

287 In Fig. 5(d), v_* , r_* , and C_{bc} are held fixed and the detector focus position s is varied. As s increases,
 288 the signal peak arrives later and becomes more faint. However, as time passes, all signals converge as light
 289 spreads within the medium and the distribution of emitted photons becomes nearly uniform across the
 290 observed region.

291 Algorithm

292 We fit functions of the same form as Eq. 5 to two photon time-of-flight histograms—each measured using a
 293 different laser wavelength. We implement a grid search algorithm to find the fit parameters that minimize
 294 a negative log-likelihood loss function that properly accounts for photon count statistics. The parameters
 295 of the fitted curves are then used to compute the snowpack properties v_* , r_* , and C_{bc} . A visualization of
 296 our retrieval algorithm is shown in Fig. 6.

297 *Fit Parameterization*

298 We re-parameterize Eq. 5 in terms of the fitting parameters $\alpha' = \frac{\alpha c_*}{3(2\pi)^{3/2}}$, $\beta = \mu_a c_*$, $\gamma = 2Dc_*$, and
 299 $\delta = z_0^2$. This allows for the model to be expressed in simplified form:

$$R(s, t) = \alpha' \frac{\delta}{(\gamma t)^{5/2}} \exp\left(-\beta t - \frac{s^2 + \delta}{2\gamma t}\right) \left[1 + \frac{7}{3} \exp\left(-\frac{20\delta}{9\gamma t}\right)\right]. \quad (13)$$

300 Although Eq. 13 appears to have four degrees of freedom, only the exponential decay rate parameter β
 301 and the spatial spread rate γ are used to estimate snowpack properties in practice. Interpreting the scaling
 302 constant α' requires precise calibration of the instrument and measurement geometry which is challenging
 303 in practice and which we did not attempt. Eq. 13 also depends only weakly on the squared source depth
 304 δ , to the point that accurate estimates of δ are almost never obtained.

305 The relative contributions of v_* and C_{bc} to the decay rate parameter β vary significantly as a function of
 306 wavelength. However, for visible and near infrared light ($\lambda \lesssim 1100$ nm), the spatial spread rate γ depends
 307 primarily on μ'_s and c_* , which are largely independent of the measurement wavelength. Altogether, this
 308 means that $n + 1$ independent parameters can be retrieved from measurements taken at n wavelengths. If
 309 absorption due to light absorbing particles is known to be insignificant (i.e. $\mu_a^{bc} \ll \mu_a^{ice}$), then v_* and r_*
 310 can be retrieved from measurements at a single wavelength. Otherwise, retrieving v_* , r_* , and C_{bc} requires
 311 measurements at two or more wavelengths.

312 *Maximum Likelihood Estimate of Model Parameters*

313 The number of counts in a histogram timing bin centered at t_i is assumed to be a Poisson random variable
 314 with a rate parameter x_i , defined as

$$x_i = R(s, t_i; \Theta) + \eta = \alpha' r_i + \eta, \quad (14)$$

315 where R is the flux predicted by Eq. 13 at position s , time t_i , and for parameters $\Theta = \{\alpha', \beta, \gamma, \delta\}$.
 316 The rate of background counts produced by ambient light, detector dark counts, and detector afterpulsing
 317 (Zappa and others, 2007) is denoted by η , and is assumed to be constant with respect to time. The variable
 318 r_i denotes the normalized predicted flux, for which $\alpha' = 1$.

319 The probability of observing a vector of time-binned photon counts \mathbf{y} given a vector of predicted count
 320 rates \mathbf{x} is

$$P(\mathbf{y}|\mathbf{x}) = \prod_{\Delta}^N \frac{x_i^{y_i} e^{-x_i}}{y_i!} \quad (15)$$

321 where N denotes the total number of timing bins in the histogram and Δ is the starting bin for the
 322 curve fit. We seek to find the parameters $\Theta = \{\alpha', \beta, \gamma, \delta\}$ and η that minimize the negative log-likelihood

$$\begin{aligned} \mathcal{L}(\Theta, \eta|\mathbf{y}) &= -\ln P(\mathbf{y}|\mathbf{x}(\Theta, \eta)) \\ &= \sum_{\Delta}^N x_i - y_i \ln x_i + \ln y_i!. \end{aligned} \quad (16)$$

323 We minimize Eq. 16 using a grid search. To reduce the dimensionality of the search, we first estimate η
 324 by computing the mean number of counts in a designated set of noise bins that reliably contains effectively
 325 zero non-background counts. For any combination of β , γ , and δ , the scaling term α' can then be estimated
 326 using the expression $\bar{\alpha}' = \sum_{\Delta}^N (y_i - \eta) / \sum_{\Delta}^N r_i$.

327 We can thus define a three-dimensional search area that contains all feasible values of β , γ , and δ . The
 328 feasible range for δ is tightly constrained to $\left(\frac{3\gamma}{2c_0}\right)^2 < \delta < \left(\frac{3n_{ice}\gamma}{2c_0}\right)^2$, which allows for a coarse fit to be
 329 obtained using an effectively two-dimensional search. We uniformly sample the search area to create a grid
 330 of candidate fit parameters, and compute the negative log-likelihood for each set of parameters on the grid.

331 We perform a sequence of nested searches—we first obtain a coarse fit, then define a small search range
 332 around the fitted parameters and repeat the search using a smaller grid cell size. This procedure is iterated
 333 until a fit with the desired precision is obtained. Our fitting algorithm was implemented in MATLAB on
 334 a Lenovo Thinkpad T590 laptop with 16GB of RAM. Run time per fit was typically 56 seconds for 640
 335 nm histograms, and 19 seconds for 905 nm histograms (which had fewer timing bins). Curve fits obtained
 336 using our algorithm are shown in Fig. 6. We estimated the uncertainty in the retrieved values of β , γ , and
 337 δ by computing the inverse of the Hessian of the loss function at the estimated minimum, and then taking
 338 the diagonal terms. These terms approximate the variances in parameter fits when the loss function is
 339 approximately Gaussian near the minimum (Bevington and Robinson, 1992).

340 *Computing v_* , r_* , and C_{bc}*

341 When measurements are obtained at two wavelengths, λ_1 and λ_2 , the ice volume fraction v_* and black
 342 carbon mixing ratio C_{bc} can be extracted from the decay parameters β_1 and β_2 . Each term β_i can be
 343 expressed as a function of v_* and C_{bc} by taking the product of Eqs. 9 and 11. This results in a set of two
 344 equations which can be solved, first, for v_* :

$$v_* = \frac{b_2\beta_1 - b_1\beta_2}{c_0(a_1b_2 - a_2b_1) - d_1b_2\beta_1 + d_2b_1\beta_2}. \tag{17}$$

345 For notational simplicity we have made the substitutions $a_i = B\Gamma_i$, $b_i = \rho_{ice}MAE_{bc}(\lambda_i)$, and $d_i =$
 346 $n_{ice}(\lambda_i)B - 1$. As before, the term c_0 refers to the speed of light in air.

347 Once v_* has been obtained, C_{bc} can be computed as follows:

$$\begin{aligned} C_{bc} &= \frac{1}{c_0b_1(1 + fv_*)} \left[\left(\frac{1}{v_*} + d_1 \right) \beta_1 - c_0a_1 \right] \\ &= \frac{1}{c_0b_2(1 + fv_*)} \left[\left(\frac{1}{v_*} + d_2 \right) \beta_2 - c_0a_2 \right]. \end{aligned} \tag{18}$$

348 Here we have substituted $f = B - 1$. After v_* and C_{bc} have been computed, the grain radius r_* can be
 349 computed from the spatial spread parameter γ_i at either wavelength:

$$r_* = e_i \left[\frac{2c_0}{3\gamma_iv_*(1 + d_iv_*)} - a_i - b_iC_{bc}(1 + fv_*) \right]^{-1}. \tag{19}$$

350 Here a_i , b_i , d_i and f are defined as they were previously, and $e_i = 3(1 - g)/2$. Because r_* can be
 351 computed using either γ_1 or γ_2 , we evaluate Eq. 19 at both wavelengths, and then take the uncertainty-

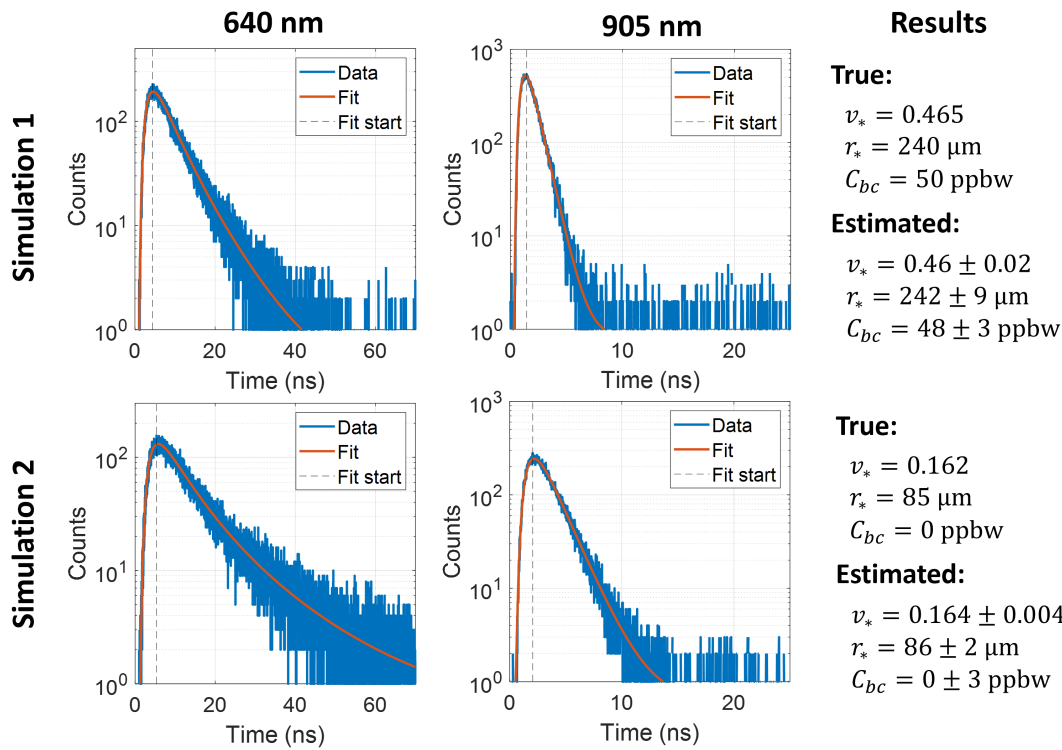


Fig. 7. We used a monte-carlo photon transport simulator to validate our retrieval algorithm. Measurements were simulated for 640 nm (left) and 905 nm (center) light for two simulated snow samples. True and estimated snowpack parameters for each sample are shown on the right.

352 weighted average of the two values obtained in this way to arrive at our final estimate for r_* . Uncertainties
 353 in v_* , r_* , and C_{bc} are obtained via error propagation from uncertainties in β_1 , β_2 , γ_1 , and γ_2 .

354 If it is known that absorption by light absorbing particles is small compared to absorption by ice grains,
 355 then v_* and r_* can be computed from the fit parameters extracted from single-wavelength measurements.
 356 First v_* can be computed from the exponential decay rate β , as follows:

$$v_* = \frac{\beta}{ac_0 - \beta d}, \tag{20}$$

357 and then r_* can be obtained from the spatial spread rate γ , and our estimate of v_* :

$$r_* = e \left[\frac{2c_0}{3\gamma v_*(1 + dv_*)} - a \right]^{-1}. \tag{21}$$

358 Here a , b , d , and e retain their meanings from Eqs. 17 and 19.

359 Evaluation Using Simulated Measurements

360 We validated our algorithm using a GPU-accelerated Monte-carlo photon transport simulation (Henley,
 361 2020), which was adapted from a simulator originally developed for tissue imaging studies (Satat, 2019).
 362 We modeled the propagation of photons within a semi-infinite, homogeneous scattering medium. The
 363 medium's properties μ_a , μ'_s , and c_* were computed from v_* , r_* , and C_{bc} using Eqs. 7, 9, and 11. To

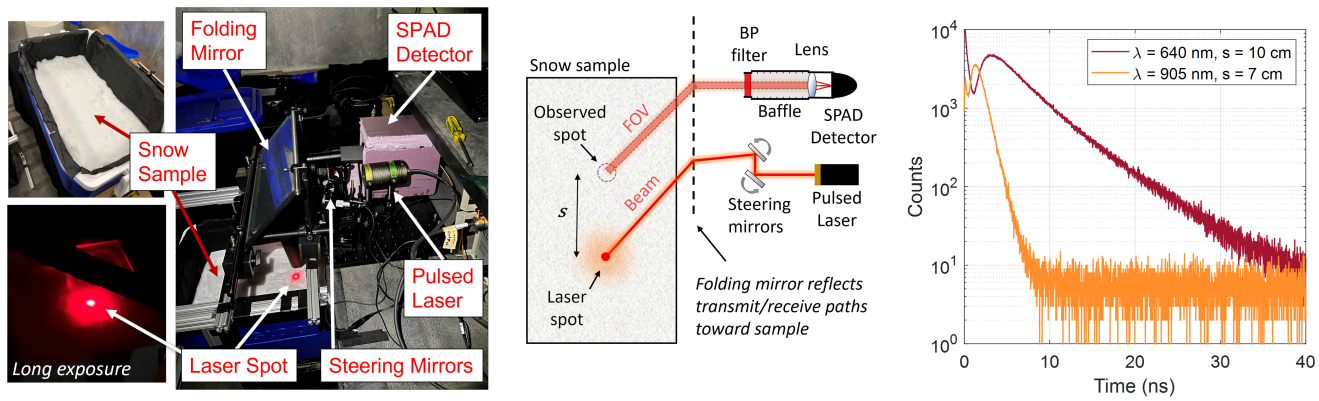


Fig. 8. (Left) Photos depicting our experimental setup. Snow was held in a cooler placed on the floor, and illuminated using pulsed diode lasers at two wavelengths (640 nm, 905 nm). A single-photon avalanche diode (enclosed in pink insulating foam) measured the time-of-flight of photons that exited the snow surface at distance s from the laser spot. (Center) Schematic of experimental setup. (Right) Time-of-flight histograms measured using our system. For this test the snow sample consisted of natural snow that had been aged for nine months at $-10\text{ }^{\circ}\text{C}$.

364 simulate pencil-beam illumination, photons were launched at the origin ($[x, y, z] = \mathbf{0}$) at time $t = 0$ and at
 365 normal incidence to the snow surface. Photons scattered randomly in the medium until they were absorbed,
 366 exited the medium, or satisfied an outlier termination criterion such as maximum number of scattering
 367 events. For more details, we refer the reader to Chapter 4 of Welch and van Gemert (1995).

368 We simulated photon time-of-flight histograms at 640 nm and 905 nm measurement wavelengths for
 369 two snow samples with different properties. We binned photons by the transverse position s (bin width
 370 1 cm) and time t (bin width 16 ps) that photons exited the snow surface. In the first simulation, for 640
 371 nm measurements, photons detected at $s = 8.0 \pm 0.5$ cm were used for curve fitting, whereas for 905 nm
 372 measurements photons detected at $s = 5.0 \pm 0.5$ cm were used. In the second simulation, for 640 nm
 373 measurements, photons detected at $s = 10.0 \pm 0.5$ cm were used for curve fitting, whereas for 905 nm
 374 measurements photons detected at $s = 7.0 \pm 0.5$ cm were used. Once a histogram of signal photons was
 375 created, a random number of background counts was added to each timing bin by sampling from a Poisson
 376 distribution with rate parameter η that was chosen to be consistent with the uniform background count
 377 levels observed in experimental measurements.

378 Our results are shown in Fig. 7. For the first simulation, the true snowpack properties were $v_* = 0.465$,
 379 $r_* = 240\text{ }\mu\text{m}$, and $C_{bc} = 50$ ppbw. Our method retrieved values of $v_* = 0.46 \pm 0.02$, $r_* = 242 \pm 9\text{ }\mu\text{m}$, and
 380 $C_{bc} = 48 \pm 3$ ppbw. For the second simulation, the true snowpack properties were $v_* = 0.162$, $r_* = 85\text{ }\mu\text{m}$,
 381 and $C_{bc} = 0$ ppbw. Our method retrieved values of $v_* = 0.164 \pm 0.004$, $r_* = 86 \pm 2\text{ }\mu\text{m}$, and $C_{bc} = 0 \pm 3$
 382 ppbw. These results suggest that our algorithm should produce accurate estimates under the idealized
 383 conditions prescribed here, and if our snow scattering model is correct.

384 MATERIALS

385 Apparatus

386 Lidar System

387 We assembled a simple lidar system to measure the time-domain optical response of a variety of snow
388 samples. We perform time-correlated single-photon counting, in which a histogram of photon times of
389 flight is built up over time by repeatedly illuminating the snow surface with a pulsed laser. Photographs of
390 our experimental setup are shown on the left in Fig 8. Our lidar system used a single-pixel SPAD detector
391 (Microphoton Devices PDM series) with a timing jitter of ~ 50 ps (FWHM), and two pulsed diode laser
392 sources—a red laser with a wavelength of 640 nm (Picoquant LDH-P-C-640B), and a near-infrared laser
393 with a wavelength of 905 nm (Picoquant LDH-P-C-905). Each laser was operated at a pulse repetition
394 frequency of 2.5 MHz and had a quoted pulsewidth of < 90 ps. The 640 nm laser was operated at a
395 time-averaged power of $80 \mu\text{W}$, and the 905 nm laser was operated at a time-averaged power of $55 \mu\text{W}$.
396 A Picoquant Hydraharp 400 was used to synchronize the arrival times of detected photons with the laser
397 repetition rate. The overall instrument response function (IRF) of the system was measured to be 128 and
398 160 ps (FWHM) for 640 and 905 nm measurements, respectively.

399 Measurement Procedure

400 Experiments were conducted in a cold room at -1°C . The room's lights were switched off and windows
401 blacked out to reduce interference from ambient background light. A large folding mirror was used to direct
402 the lidar beam and detector field of view (FOV) towards a cooler filled with snow that was placed on the
403 floor. A schematic that illustrates our system's optical design is shown in the center of Fig. 8. Because only
404 a single laser diode could be operated at any one time, 640 nm measurements were collected first. During
405 these measurements, a red bandpass filter (Edmund Optics TECHSPEC 650nm/50nm) was placed in front
406 of the detector to suppress interference from ambient background light. Following these measurements
407 the 640 nm laser head and bandpass filter were removed and replaced with the 905 nm laser head and a
408 near-infrared bandpass filter (Thorlabs FL905-10). We then collected a second set of measurements.

409 The beam from either laser head could be scanned by hand using a set of steering mirrors. A lens was
410 placed in front of the detector to focus its FOV to a small spot (< 1 cm FWHM) on the snow surface. To
411 find this focus spot, the laser beam would be steered to the point on the surface at which detector counts
412 were maximized. Once the focus spot was found, a laser pointer (distinct from the pulsed diode lasers) was
413 steered to mark the position of the focus spot. The *pulsed* beam could then be steered to a point on the
414 snow surface that was displaced from the focus spot by a small distance s that was measured using a ruler.
415 The focus-marker beam would then be switched off. When the 905 nm laser was in use, a phosphorescent
416 laser viewing card was used to find the position of the laser spot on the snow surface.

417 We note that even when the laser and focus spots were separated by several centimeters, interference
418 from direct returns off of the snow surface remained significant due to phenomena such as lens flare.
419 Although we could not suppress this interference entirely, we were able to mitigate it by placing a long lens
420 tube in front of our detector that functioned as a baffle. When possible, we would further reduce interference

421 by placing a larger tube (5 cm diameter) constructed from blackout material (Thorlabs BKF12) on the
422 snow surface, surrounding the spot observed by the detector. Together, these two baffles blocked most light
423 paths that scattered off of the snow surface while transmitting paths that traveled beneath the surface.

424 For each snow sample, and for each laser wavelength, we collected measurements at multiple source-
425 detector separations s . Each measurement consisted of a histogram of photon arrival times with 16 ps
426 timing bins that spanned a 250 ns timing window. Examples of histograms measured by our lidar system
427 are shown on the right in Fig. 8. The first measurement would always be collected at $s = 0$ cm to measure
428 the time-of-arrival of photons that scattered directly off of the snow surface. The peak of this direct
429 return would serve as a reference time for all subsequent measurements. Direct surface returns were always
430 measured with a 60 second integration time, with a neutral density filter placed in front of the detector
431 to prevent saturation, and with a wooden ruler placed on the snow surface at the position of the laser
432 spot to prevent bias due to subsurface scattering. Following this, histograms would be collected for one or
433 more non-zero source-detector separations. We used an integration time of 10 minutes for each histogram
434 collected with 640 nm light, and 30 minutes for each histogram collected with 905 nm light. A longer
435 integration time was required at 905 nm because our SPAD detector was less sensitive at this wavelength,
436 the output power of our laser was lower, and the snow itself was less reflective. Ice grains from each sample
437 were inspected before and after each set of measurements to ensure that snow properties had not changed
438 significantly due to metamorphism.

439 Before proceeding, we want to stress that our lidar system was assembled strictly for the proof-of-
440 principle demonstrations documented in this paper. It was not optimized for ease of use or light collection
441 efficiency. Although the integration times reported here are quite long, we expect that a cleverly engineered
442 system might collect equivalent data with integration times that are far shorter—perhaps by several orders
443 of magnitude. Integration time could be reduced significantly, for instance, by using a multipixel Silicon
444 Photomultiplier (SiPM) in place of the single-pixel SPAD used here, and by using lasers with higher power
445 and higher repetition rates. The use of laser sources and SPADs designed for a consumer electronics
446 environment (King and others, 2023), rather than the optical bench equipment used here, would also allow
447 for a system that was portable, rugged, and affordable. Altogether, this suggests that the development of
448 a field-deployable system is a feasible goal—one which we hope to pursue in future work.

449 Samples

450 We performed two sets of experiments. In the first, samples had relatively low LAP concentrations but
451 grain size and density varied significantly. In the second, the samples had varying amounts of black carbon
452 mixed into them, but density and grain size was relatively constant.

453 All snow used in our experiment originated as natural snow harvested on Dartmouth College campus
454 and was subsequently modified in various ways. When not being used for experiments, snow samples were
455 stored in lidded coolers in a -10 °C cold room.

456 *Clean Snow Samples*

457 We performed five sets of measurements on samples with varying density and grain size but relatively low
458 LAP content. The snow used in the first set of measurements was harvested after a snowfall in March
459 2022 and then kept in a $-10\text{ }^{\circ}\text{C}$ cold room for nine months. By the time measurements were taken, the
460 snow had become more dense and the grains had metamorphosed into medium size rounded grains and
461 rounding faceted particles (Fierz and others, 2009). The next three data collections were performed on
462 a single snow sample that was modified between measurements. The sample was harvested 30 minutes
463 after snow had ceased falling, immediately outside our laboratory at Dartmouth College. It was then
464 stored overnight at $-10\text{ }^{\circ}\text{C}$. Measurements were collected the next morning on the unmodified sample,
465 which had a very low density and consisted of precipitation particles (Fierz and others, 2009), with many
466 stellar dendrites. A second set of measurements was collected after the snow had been compacted with a
467 shovel—thus increasing its density and potentially reducing grain size by fragmenting grains. The third
468 set of measurements was collected after the snow was aged for three weeks at $-10\text{ }^{\circ}\text{C}$ and then for one
469 day at $0\text{ }^{\circ}\text{C}$. This aging produced a clear change in grain shape, to small rounded grains and decomposing
470 precipitation particles, and a small increase in grain size and density. For our final set of measurements we
471 harvested snow that had been sitting outside for weeks, where it had experienced several melt and re-freeze
472 events. This snow had very high density and coarse grains.

473 At the time of data collection, all samples were held in coolers with approximate internal dimensions
474 of $50\text{ cm}\times 25\text{ cm}\times 30\text{ cm}$ and that had matte white internal walls. Snow would fill the cooler to varying
475 degrees, but was typically at least 20 cm deep, relative to the cooler bottom.

476 *Soot Addition Experiments*

477 For the second set of experiments, we filled five Styrofoam coolers (dimensions $17.5\text{ cm}\times 23.5\text{ cm}\times 24.0\text{ cm}$)
478 with freshly fallen snow. We then mixed small amounts of Sigma-Aldrich Fullerene Soot (PN: 572497) into
479 the samples, such that the five respective samples had 0, 1, 2, 3, and 4 baseline units of soot. To add
480 soot to the snow in a controlled fashion, we created a soot-water suspension with a known concentration
481 of soot, and then applied controlled volumes of the suspension to each snow sample with a spray bottle.
482 The soot was mixed evenly into the snow using an ice scraper.

483 After performing a first set of measurements on the sooty samples we found that the added soot had a
484 weaker effect on the snowpack absorption coefficients than had been expected. Following this finding, we
485 approximately doubled the added soot concentration in all samples and repeated the measurements.

486 **Ground Truth Measurements**

487 Ground truth ice volume fraction was measured by extracting a small core with a depth of $\sim 5\text{ cm}$ and
488 diameter of $\sim 6\text{ cm}$ from the snow surface using a cylindrical polypropylene jar. We measured the volume
489 of snow in the core. The snow was then allowed to melt, and we measured the volume of the meltwater.
490 Ice volume fraction was computed from the snow and meltwater volumes using conservation of mass.

491 Ground truth grain size was measured by imaging a small, snow-filled test tube (1.4 cm internal
492 diameter) with a SkyScan 1172 microCT scanner (40 kV, 250 μA source, 17 μm resolution). Bruker

493 NRecon software was used to reconstruct a 3D image of the sample. Following guidance from Hagenmuller
494 and others (2016), the image was then blurred with a Gaussian kernel (radius 1 pixel), binarized with
495 Otsu's method, and morphologically "opened" (radius 1 pixel). The surface area to volume ratio (SA/V)
496 of the imaged sample was then computed two times using Bruker's CTAN software, following marching
497 squares (2D analysis) and marching cubes (3D analysis) surface reconstructions. We computed the grain
498 radius from each SA/V ratio independently, and then used the average of these two values as ground truth.

499 Ground truth estimates of black carbon concentration were obtained using a single particle soot pho-
500 tometer (SP2; Droplet Measurement Technologies), in a manner similar to that reported in Lazarcik and
501 others (2017). Each snow sample was melted and ultrasonicated for at least 15 minutes prior to analy-
502 sis. The liquid snow samples were aerosolized using an ultrasonic nebulizer (CETAC U5000AT), which
503 removes moisture from the liquid stream before passing aerosols such as black carbon onto the SP2. The
504 SP2 estimates black carbon particle mass via measurements of laser-induced incandescence. This system
505 was calibrated using a series of fullerene soot standards. To avoid saturating the SP2, snow samples that
506 were expected to have particularly high black carbon concentrations were diluted with MilliQ water by a
507 factor of 6.

508 RESULTS

509 Clean Snow Experiments

510 *Individual Snow Sample*

511 To provide insight into our data collection and fitting procedures, we first present a detailed review of all
512 measurements collected for a single snow sample. This sample, which is described in greater detail in the
513 Materials section, consisted of natural snow that had been aged for nine months in a -10 °C cold room.

514 The raw, time-of-flight histogram data collected for this sample, as well as our curve fits to those
515 measurements, are shown in Fig. 9. Measurements were taken at four different source-detector separations
516 for each wavelength: $s = 4, 6, 8$ and 10 cm at 640 nm, and $s = 4, 5, 6$ and 7 cm at 905 nm. As a rule
517 of thumb, we would start each fit at a timing bin that corresponded to the peak of the diffusion signal.
518 This was done to avoid fitting to the earliest arriving photons, which are poorly described by our diffusion
519 model. Histograms were collected at multiple s values because it was not known *a priori* what range of
520 s values would yield good diffusion curve fits. If s and μ'_s were both small, then photons in the signal
521 peak would be poorly described by our diffusion model because they would exit the snowpack after too
522 few scattering events. On the other hand, if s and μ'_s or μ_a were too large, the diffusion signal would be
523 faint relative to background interference, and the fit would be poor.

524 In Fig. 10, we show how the retrieved snow properties varied with respect to our choices of source-
525 detector separation at each wavelength. In general, estimates of v_* , r_* , and C_{bc} did not vary substantially
526 if good curve fits were obtained at both wavelengths, but diverged from the typical value when one or both
527 of the curve fits were poor. As an example, it is evident in Fig. 10(c) that C_{bc} estimates are biased high
528 at $s_{640} = 4$ cm, but are otherwise relatively insensitive to changes in s at either wavelength. A relatively
529 small amount of variance was observed in snow property estimates even when good fits were obtained.
530 The sources of this variance are unconfirmed, but could be explained by instrumental phenomena such as

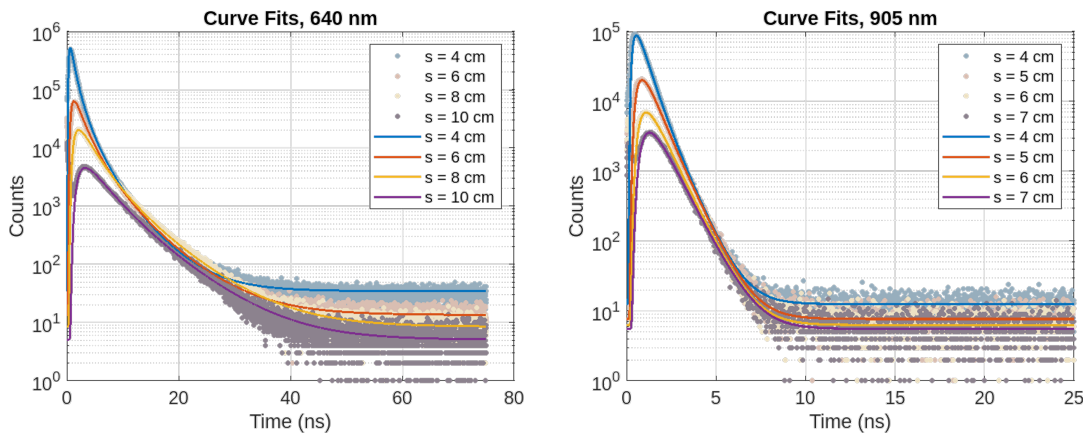


Fig. 9. Raw measurements collected for a single snow sample. Time-of-flight histograms were measured at two wavelengths (640 nm, 905 nm) and for four source-detector separations per wavelength. A diffusion model was fit to each histogram. The pair of curves with the best goodness of fit was used to compute snowpack properties.

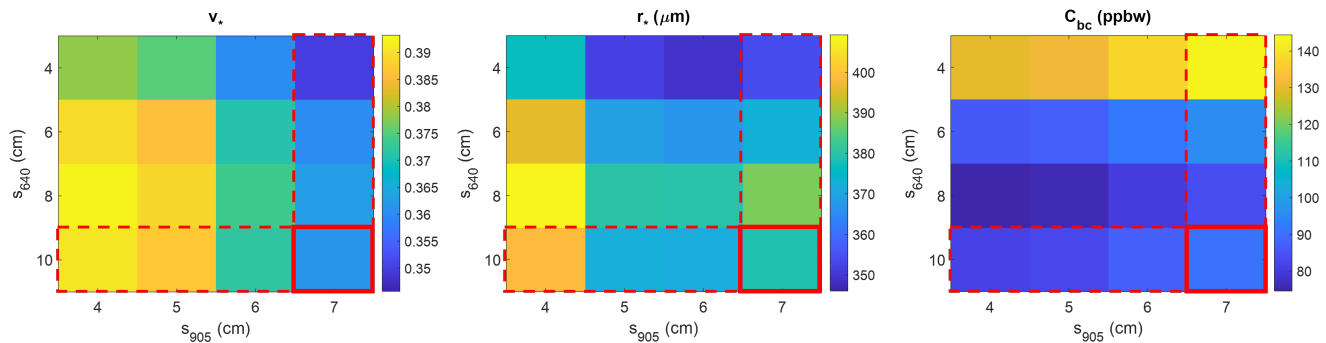


Fig. 10. Dependence of v_* , r_* , and C_{bc} estimates on choice of source-detector separation s for each measurement wavelength. Estimates that correspond to the pair of curve fits with the lowest reduced deviance (McCullagh, 2019) are outlined in red.

531 photon pile-up distortion (Coates, 1968); the varied influence of unmodelled phenomena such as surface
 532 roughness, finite cooler size, or interference from direct surface returns; the metamorphism of snow between
 533 data collections; or true spatial variation in the snow’s properties.

534 To arrive at a single estimate for v_* , r_* , and C_{bc} , we chose the curve fit at each wavelength with the
 535 lowest *reduced deviance* (McCullagh, 2019). Deviance is a goodness of fit metric that is appropriate for data
 536 that follows Poisson statistics, and that is asymptotically equivalent to χ^2 goodness of fit when the number
 537 of counts in all histogram bins is high. For the data collection described here, the best fits corresponded
 538 to $s = 10$ cm at 640 nm and $s = 7$ cm at 905 nm. From the parameters of these two fits we estimated
 539 that $v_* = 0.361 \pm 0.004$, $r_* = 379 \pm 4$ μm , and $C_{bc} = 91 \pm 1$ ppbw. As described previously, the reported
 540 uncertainties correspond to statistical uncertainties in the curve fit parameters, propagated through Eqs.
 541 17, 18, and 19. They do not account for potential inaccuracies in the diffusion or scattering models. The
 542 ground truth measurements of v_* , r_* , and C_{bc} were 0.465, 242.5 μm , and 30.7 ppbw, respectively.

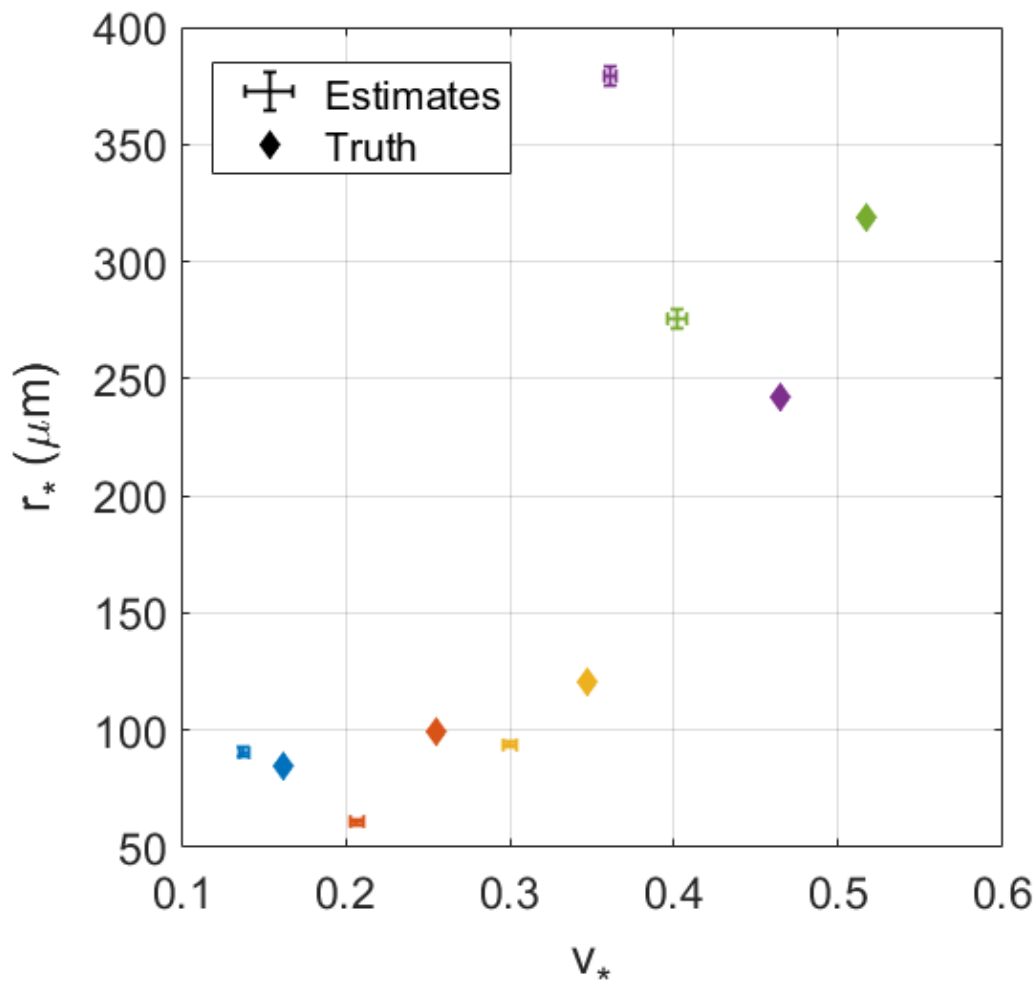


Fig. 11. Summary of the estimated and ground truth ice volume fractions v_* and grain sizes r_* of five clean snow samples. Error bars indicate one standard deviation. Estimates and ground truth values are matched by color.

543 Full Results

544 We now present a summary of all results obtained for the clean snow samples. The properties of the snow
 545 samples used in these tests varied widely, from light, fine-grained fresh powder to dense, coarse-grained
 546 snow that had experienced several melt and re-freeze events. In Fig. 11, we show a scatter plot of the
 547 densities and grain sizes estimated using our method, as well as ground truth values.

548 Our estimates of v_* , r_* , and C_{bc} are plotted with respect to ground truth in Fig. 12. In Fig. 12(a),
 549 we see a clear positive and nearly linear relationship between the ice volume fraction estimated using our
 550 technique, and ground truth, although estimates appear to be biased towards lower densities. The trends
 551 for r_* and C_{bc} are less clear, although our method appears to be capable of distinguishing between small
 552 and large grain sizes, and low and moderate impurity concentrations. To the extent that trends can be
 553 observed, there appears to be an approximately 1:1 relationship between r_* estimates and ground truth,
 554 whereas C_{bc} appears to be over-estimated by a factor of ~ 2.5 . All statistical uncertainties in v_* and r_*

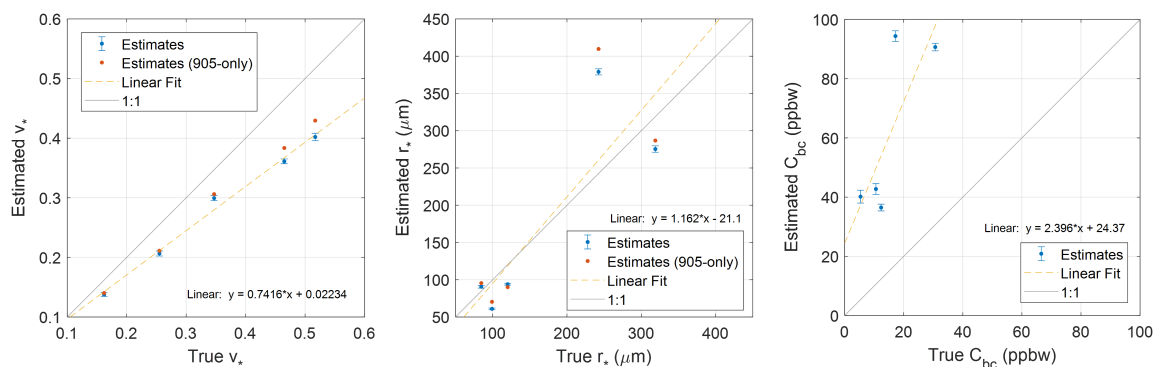


Fig. 12. Ground truth versus estimated values of ice volume fraction v_* , grain size r_* , and black carbon mass mixing ratio C_{bc} for five clean snow samples. Blue marks indicate estimates obtained using two measurement wavelengths (640 nm, 905 nm). Error bars indicate one standard deviation. Red marks indicate estimates of v_* and r_* obtained from 905 nm measurements only. Uncertainties were not computed for 905-only estimates.

555 estimates are 1-2% of the estimated value. All statistical uncertainties in C_{bc} estimates are 1-2 ppbw.
 556 Notably, these uncertainties are comparable to the statistical uncertainties reported by Allgaier and others
 557 (2022) in their estimates of black carbon concentrations in glacier ice.

558 In addition to dual-wavelength estimates of v_* , r_* , and C_{bc} , we also show estimates of v_* and r_* computed
 559 using only 905 nm measurements. The single-wavelength results match the dual-wavelength results very
 560 closely. Ice volume fraction estimates are slightly higher, which is consistent with excess absorption due to
 561 unmodeled LAPs. Single-wavelength grain size estimates are alternately higher or lower than corresponding
 562 dual-wavelength estimates.

563 Considering the very small statistical uncertainties in our results, we expect that the biases seen here
 564 are most likely attributable to model mismatch. In particular, the excess black carbon content predicted
 565 by our method is plausibly explained by the presence of other kinds of light absorbing impurities such as
 566 dust. The samples used in this test were collected outdoors and were handled with shovels, ice scrapers,
 567 and various other equipment that may have been coated with dust or dirt. Further investigation is needed
 568 to understand the bias in estimates of v_* , which appear to be underestimated by a factor of approximately
 569 3/4. One possible explanation is that the measured signal was influenced by unmodeled reflections from
 570 the white side-walls of the cooler. A deeper analysis would be required to confirm this. However, one would
 571 expect such reflections to reduce the observed decay rate by scattering photons back into the probed region
 572 instead of allowing them to escape. There is a notable outlier among the r_* estimates that is approximately
 573 50% higher than its ground truth measurement (estimate: $379.0 \pm 4.1 \mu\text{m}$, truth: $242.5 \mu\text{m}$). The origins
 574 of this outlier are unclear. By inspection of Eq. 7, we see that the estimated r_* value would be reduced by
 575 50% if the modeled scattering asymmetry factor was increased from 0.825 to 0.883. It is thus possible that
 576 the outlier snow sample—which consisted of medium size rounded grains and rounding faceted particles
 577 that had been aged for nine months in a $-10 \text{ }^\circ\text{C}$ cold room—had a higher scattering asymmetry factor
 578 than the others. However it is not clear why this would be so.

579 Soot Addition Experiments

580 Here we present the results of the soot addition experiments described in the Materials section, where
581 the snow samples contained varying concentrations of black carbon. For these tests, the source-detector
582 separation was held fixed at $s = 8$ cm for 640 nm measurements. For 905 nm measurements, a value of s
583 $= 5$ cm was typically used, although this was occasionally reduced to 4 cm if the measured signal would
584 otherwise be too faint to yield a good curve fit.

585 The primary goal of these experiments was to assess the accuracy and sensitivity of the estimates of
586 black carbon mass mixing ratio produced by our method. To this end, in Fig. 13 we show a plot of the C_{bc}
587 values estimated with our method versus ground truth estimates obtained using an SP2. Blue data points
588 correspond to the first set of measurements, for which the soot concentrations were relatively low, and red
589 data points correspond to a second set of measurements that was collected after the added black carbon
590 concentration in each snow sample had been approximately doubled.

591 Upon inspection we see a clear correlation between the estimated and ground truth C_{bc} values. The
592 correlation is approximately linear and nearly one-to-one. Two outlier data points (with ground truth C_{bc}
593 of 58, 59 ppbw) lie off of the one-to-one line. We expect that the outliers are the result of an error in
594 the ground truth estimates. It is possible that our mixing process did not uniformly distribute the black
595 carbon content throughout the snow and that the region sampled for SP2 analysis was unusually clean.

596 The range of estimated C_{bc} values indicates that our technique is sensitive to concentrations above
597 100 ppbw. Notably, this is significantly more sensitive than estimates derived from remote, multi-spectral
598 albedo measurements, which are unreliable for black carbon concentrations below 1000 ppbw (Zege and
599 others, 2011; Warren, 2013). Methods that infer black carbon concentration from in situ, hyperspectral
600 albedo are sensitive to black carbon concentrations above 50 ppbw (Dumont and others, 2017), which is
601 comparable to the sensitivity achieved here. The sensitivity of our method could be improved, perhaps
602 significantly, by using a blue or green laser source in place of the red laser used here. As shown in Figure 4,
603 the influence of black carbon on the absorption coefficient of snow is much stronger at these wavelengths.

604 For good measure, we also show the estimates of ice volume fraction, grain radius, and black carbon
605 concentration obtained for all samples. Estimates are plotted in Fig. 14 as a function of total units of
606 soot-water solution that were applied to each sample using a spray bottle. Although ground truth v_* and
607 r_* were not collected, results in Fig. 14(a) and (b) indicate that the density and grain size of the snow
608 samples was relatively consistent, but did have some variance. This variance may have been caused by
609 differences in how each sample was mixed, or from interaction with the liquid water in the soot-water
610 suspension. Regardless, we see in Fig. 14(c) that estimated C_{bc} increases approximately linearly and nearly
611 monotonically as a function of the amount of added soot, with no clear dependence on density or grain
612 size.

613 DISCUSSION

614 In this work we have introduced a new method for measuring the density, grain size, and black carbon con-
615 tent of a dry snowpack using non-invasive, time-domain diffuse optical measurements. We have presented
616 a model for the time-domain optical response of a snowpack that was adapted from the biomedical optics

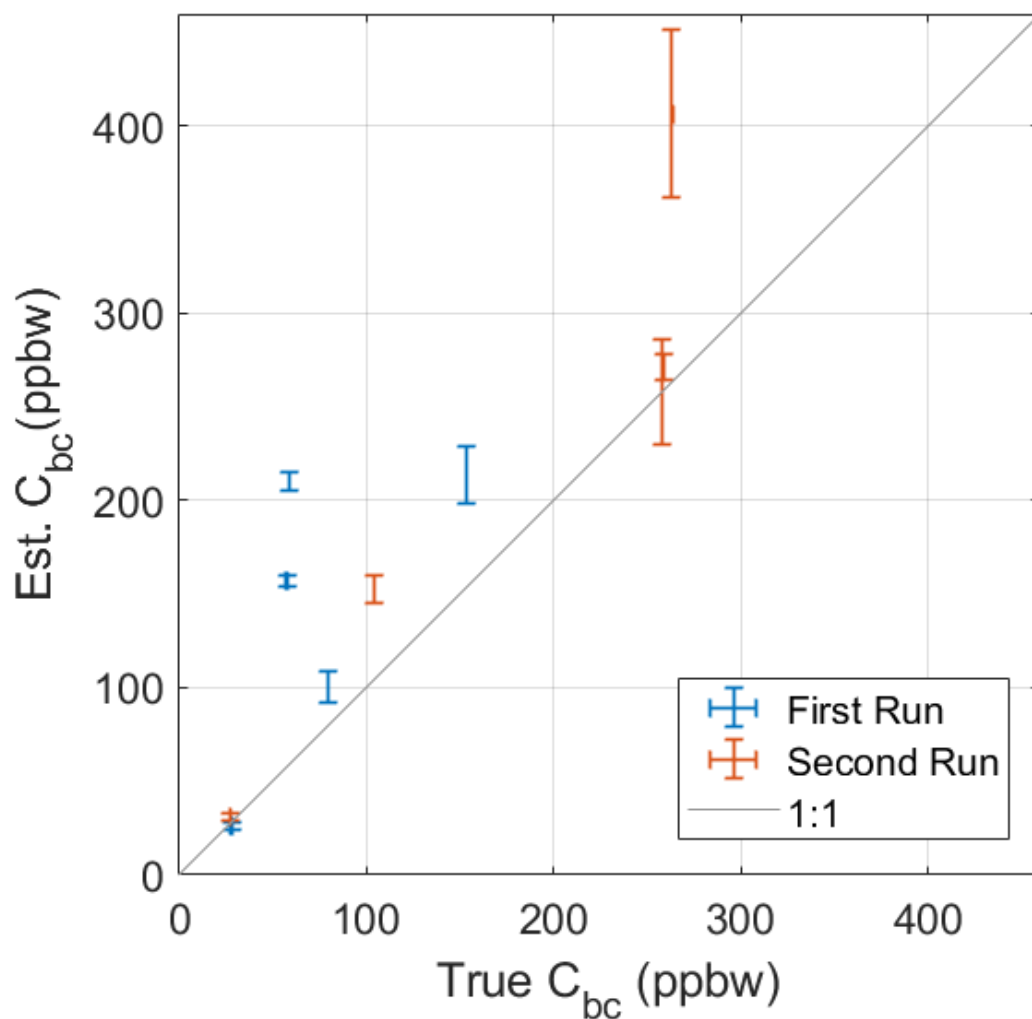


Fig. 13. Retrieved values of black carbon mass mixing ratio C_{bc} plotted with respect to ground truth estimates obtained by a single-particle soot photometer (SP2). Increasing quantities of Sigma-Aldrich fullerene soot were added to five snow samples. Results from the first set of measurements are shown in blue. Soot concentrations were then approximately doubled for all samples and a second set of measurements was taken. Results from the second set of measurements are shown in red. Error bars indicate one standard deviation. SP2 errors are typically too small to be visible.

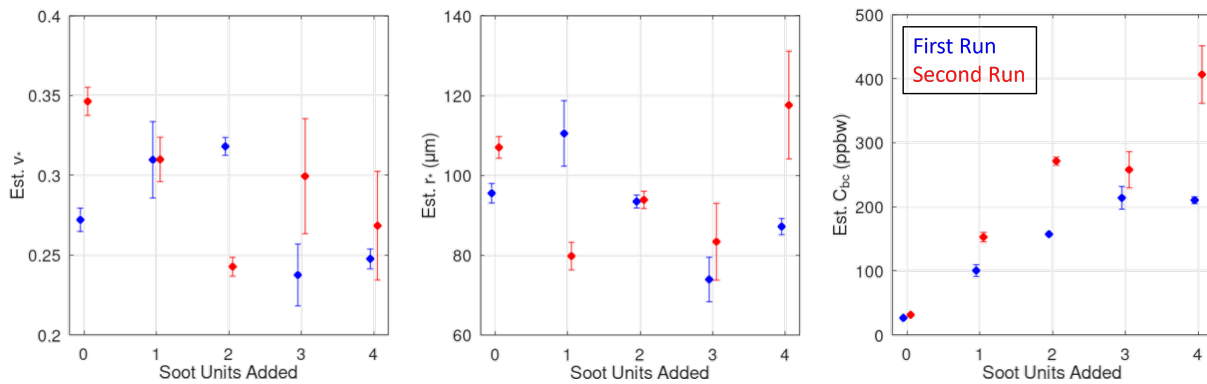


Fig. 14. Estimates of v_* , r_* , and C_{bc} obtained during soot addition experiments. Estimates are plotted as a function of the number of soot units mixed into the snow. One soot unit corresponds to a fixed volume of soot-water suspension that is applied to the snow sample with a spray bottle and then mixed into the snow volume. The amount of soot per unit in the second run (red) was approximately double the soot per unit in the first run (blue). Error bars indicate one standard deviation.

617 literature (Kienle and Patterson, 1997; Haskell and others, 1994). Our model was obtained by solving the
 618 photon diffusion equation—an approximation to the radiative transfer equation that accurately describes
 619 the propagation of light in highly scattering media (Welch and van Gemert, 1995). We used a geometric
 620 scattering model to relate the parameters of our photon diffusion model to dry snowpack density, grain
 621 size, and black carbon concentration. Our scattering model was derived from a well-known snow-optics
 622 model (Kokhanovsky and Zege, 2004), but extended to account for the effective speed of light within snow,
 623 as well as the mixing state of black carbon. We then developed an algorithm to retrieve the snowpack
 624 properties from time-domain optical measurements collected at two wavelengths.

625 We were able to validate our method in a series of proof-of-principle experiments in which we measured
 626 the properties of real snow samples using a photon-counting lidar system. The results of these experiments
 627 are encouraging. We see a clear, nearly linear correlation between the snowpack densities estimated by
 628 our method, and ground truth. When the LAPs in the snow were known to be black carbon particles,
 629 we observed a nearly one-to-one correlation between the black carbon mass mixing ratios estimated using
 630 our method, and those measured using a single-particle soot photometer (Schwarz and others, 2006). A
 631 nearly one-to-one correlation was also found between the grain sizes measured by our method and those
 632 determined from micro-CT images—although this correlation was not as strong. Our goal in this work was
 633 to obtain proof-of-principle results. More experiments are required to comprehensively assess our method's
 634 accuracy, biases, and failure modes.

635 Although our results are encouraging, we believe that the primary contribution of our work is not nec-
 636 essarily the exact method that we have proposed, but rather that we have been able to clearly demonstrate
 637 that time-domain diffuse optics is an appropriate sensing modality for measuring snowpack properties.
 638 Previous works have used ray-tracing simulations to explore the feasibility of inferring snow properties
 639 from time-domain diffuse optical signals (Libois and others, 2019), and to predict the relationship between
 640 snow properties and lidar altimetry biases (Smith and others, 2018). However, as far as we are aware, our
 641 work is the first to provide clear *experimental* evidence that the optical response of a snowpack that has
 642 been illuminated by a laser pulse can be accurately described using a photon diffusion model; and also

643 that this response is measurably influenced by changes to important snowpack properties like grain size,
644 density, and impurity content.

645 Our method could be improved in several ways. More sophisticated models that incorporate features
646 such as liquid water content in the snow, finite snow depth, or surface roughness might be developed to
647 enable retrieval of snow properties in a broader set of circumstances. Our measurement procedure could also
648 be improved. In our experiments, processing a single snow sample required between 40 minutes to several
649 hours of data collection time. This could be dramatically reduced by improving our instrument design to
650 incorporate multi-pixel SPAD detectors, higher power lasers, or by simply placing the laser and detector
651 closer to the snow surface. The integration times used in our experiments were also conservative—further
652 analysis could determine the minimum number of photons required to accurately retrieve snow properties.
653 Finally, using our method in the field would require the development of a rugged and portable instrument.
654 The dramatic decrease in the cost and size of pulsed lasers and photon counting detectors in recent years
655 makes this possible. All components required for such a device can be found in the current model of the
656 iPhone Pro (King and others, 2023).

657 Although non-invasive, optical methods for measuring snow grain size (Nolin and Dozier, 2000; Gallet
658 and others, 2009) and LAP concentrations (Dumont and others, 2017; Allgaier and Smith, 2022) have been
659 demonstrated previously, our work provides what is, to our knowledge, the first experimental demonstration
660 of snow density estimation from non-invasive optical measurements. Previous works used ray-tracing
661 simulations to demonstrate non-invasive porosity ($= 1 - v_*$) measurements in arbitrary porous media (Libois
662 and others, 2019), or estimated snow density using invasive optical transmission measurements (Gergely
663 and others, 2010). Our method could potentially provide field measurements of snow-water-equivalent
664 (SWE)—the product of snow depth and density—or surface density, which might in turn prove useful in
665 hydrological or ecological studies, or for validating remote sensing techniques (Kinar and Pomeroy, 2015).
666 Diffuse optical methods may also enable more sensitive field measurements of LAPs, particularly if shorter
667 wavelength (e.g. blue or green) illumination is used. Field measurement of black carbon concentration from
668 snow's hyperspectral albedo has been demonstrated (Dumont and others, 2017). Our method infers black
669 carbon concentration from a decay rate parameter that is proportional to snow's absorption coefficient,
670 which is far more sensitive to impurity content than albedo. The trace concentrations of impurities found
671 in remote snowpacks reduce snow's albedo by at most a few percent (Warren, 2013) whereas, in theory, the
672 absorption coefficient of snow at green wavelengths should be *doubled* by just a few ppbw of black carbon
673 (see Fig. 4). We note that the spatially-resolved diffuse optical technique demonstrated by Allgaier and
674 Smith (2022) also infers LAP concentrations via the absorption coefficient, and so should be able to achieve
675 comparable sensitivities.

676 Although the instrument used in this study was assembled from the same components that make up
677 a typical photon counting lidar system, our measurements were effectively *in situ* because our lidar was
678 always placed within a meter of the snow's surface. In the future, we hope to develop true *remote* lidar
679 sensing techniques that are grounded in time-domain diffuse optics models. Such methods would enable
680 important capabilities such as the remote mapping of SWE or impurity concentrations. However, the leap
681 from *in situ* to remote measurements poses new challenges that include dramatically lower photon counts,
682 wider beam footprints, and confocal measurement geometries. Further analysis is required to determine

683 which snow properties can be feasibly retrieved under these conditions. An alternative direction for future
684 work is the development of more advanced algorithms for processing in situ measurements that leverage
685 decades of advances in diffuse optical spectroscopy research (Konugolu Venkata Sekar and others, 2019).
686 In particular, the adaptation of *diffuse optical tomography* methods (Okawa and Hoshi, 2023) to snow would
687 enable non-invasive retrieval of snow stratigraphy, or even full 3D mapping of snowpack properties within
688 a probed region. Observations of snow stratigraphy are often made to assess the structural stability of the
689 snowpack to predict avalanche risk, as well as the history of snow deposition and metamorphism (Nienow
690 and Campbell, 2011).

691 CONCLUSIONS

692 We have developed a new technique to estimate the density, grain size, and black carbon concentration of
693 a dry snowpack using time-resolved measurements of laser light that has scattered multiple times beneath
694 the snow surface. Our method was inspired by *diffuse optical spectroscopy* techniques that were originally
695 developed for biomedical applications. We validated our method in a series of proof-of-principle experi-
696 ments. Our results revealed strong, nearly linear correlations between our estimates of snow density and
697 black carbon concentration, and independent ground truth measurements. Additionally, our method suc-
698 cessfully distinguished between small and large grain sizes. Our results indicate that non-invasive optical
699 measurement of snow density, grain size, and black carbon concentration is possible. However, further
700 refinement of our instrument design is needed for practical field use. More broadly, our work provides the
701 first clear experimental evidence that time-dependent scattering of laser light by snow is well described by
702 a diffuse optical model. This could pave the way for future algorithms that retrieve snow properties from
703 remote lidar measurements as well as more advanced in situ techniques, such as methods that infer snow
704 stratigraphy.

705 ACKNOWLEDGEMENTS

706 We wish to thank Quentin Libois and two anonymous reviewers for their helpful comments and discussion.
707 We thank Brent Minchew and Joanna Millstein for the discussions that inspired this project and for support
708 with initial theoretical work. Andrii Murdza provided general assistance with micro-CT measurements and
709 cold room experiments. Anna Valentine prepared the snow samples used in our soot addition experiments.
710 Connor Henley was supported by a Draper Scholarship and by a grant from the Office of Naval Research
711 (N00014-21-C-1040). Any opinions, findings and conclusions or recommendations expressed in this ma-
712 terial are those of the author(s) and do not necessarily reflect the views of the Office of Naval Research.
713 Colin R. Meyer was supported by the Heising-Simons Foundation (#2020-1911), the Army Research Office
714 (78811EG), and the National Science Foundation (2024132).

715 REFERENCES

716 Ackermann M and others (2006) Optical properties of deep glacial ice at the south pole. *Journal of Geophysical*
717 *Research: Atmospheres*, **111**(D13) (doi: <https://doi.org/10.1029/2005JD006687>)

- 718 Allgaier M and Smith BJ (2021) Diffuse optics for glaciology. *Opt. Express*, **29**(12), 18845–18864 (doi:
719 10.1364/OE.425630)
- 720 Allgaier M and Smith BJ (2022) Smartphone-based measurements of the optical properties of snow. *Appl. Opt.*,
721 **61**(15), 4429–4436 (doi: 10.1364/AO.457976)
- 722 Allgaier M, Cooper MG, Carlson AE, Cooley SW, Ryan JC and Smith BJ (2022) Direct measurement of optical
723 properties of glacier ice using a photon-counting diffuse lidar. *Journal of Glaciology*, **68**(272), 1210–1220 (doi:
724 10.1017/jog.2022.34)
- 725 Bargigia I, Nevin A, Farina A, Pifferi A, D’Andrea C, Karlsson M, Lundin P, Somesfalean G and Svanberg S (2013)
726 Diffuse optical techniques applied to wood characterisation. *J. Near Infrared Spectrosc.*, **21**(4), 259–268
- 727 Bevington PR and Robinson DK (1992) *Data Reduction and Error Analysis for the Physical Sciences*, pp. 146, 190.
728 McGraw-Hill, New York
- 729 Coates PB (1968) The correction for photon ‘pile-up’ in the measurement of radiative lifetimes. *Journal of Physics*
730 *E: Scientific Instruments*, **1**(8), 878–879 (doi: 10.1088/0022-3735/1/8/437)
- 731 Doherty SJ, Dang C, Hegg DA, Zhang R and Warren SG (2014) Black carbon and other light-absorbing particles
732 in snow of central north america. *Journal of Geophysical Research: Atmospheres*, **119**(22), 12,807–12,831 (doi:
733 <https://doi.org/10.1002/2014JD022350>)
- 734 Dombrovsky LA and Kokhanovsky AA (2020) Light absorption by polluted snow cover: Internal versus external
735 mixture of soot. *Journal of Quantitative Spectroscopy and Radiative Transfer*, **242**, 106799, ISSN 0022-4073 (doi:
736 <https://doi.org/10.1016/j.jqsrt.2019.106799>)
- 737 Dumont M, Arnaud L, Picard G, Libois Q, Lejeune Y, Nabat P, Voisin D and Morin S (2017) In situ continuous
738 visible and near-infrared spectroscopy of an alpine snowpack. *The Cryosphere*, **11**(3), 1091–1110 (doi: 10.5194/tc-
739 11-1091-2017)
- 740 Durduran T, Choe R, Baker W and Yodh A (2010) Diffuse optics for tissue monitoring and tomography. *Reports on*
741 *progress in physics*, **73**(7), 076701
- 742 Fair Z, Flanner M, Neumann T, Vuyovich C, Smith B and Schneider A (2024) Quantifying volumetric scattering bias
743 in icesat-2 and operation icebridge altimetry over greenland firn and aged snow. *Earth and Space Science*, **11**(6),
744 e2022EA002479 (doi: <https://doi.org/10.1029/2022EA002479>)
- 745 Fierz C, Armstrong R, Durand Y, Etchevers P, Greene E, McClung D, Nishimura K, Satyawali P and Sokratov S
746 (2009) The international classification for seasonal snow on the ground, the international classification for seasonal
747 snow on the ground, ihp-vii technical documents in hydrology no 83, iacs contribution no 1
- 748 Flanner MG, Liu X, Zhou C, Penner JE and Jiao C (2012) Enhanced solar energy absorption by internally-mixed
749 black carbon in snow grains. *Atmospheric Chemistry and Physics*, **12**(10), 4699–4721 (doi: 10.5194/acp-12-4699-
750 2012)
- 751 Gallet JC, Domine F, Zender CS and Picard G (2009) Measurement of the specific surface area of snow using infrared
752 reflectance in an integrating sphere at 1310 and 1550 nm. *The Cryosphere*, **3**(2), 167–182 (doi: 10.5194/tc-3-167-
753 2009)

- 754 Gergely M, Schneebeli M and Roth K (2010) First experiments to determine snow density from diffuse
755 near-infrared transmittance. *Cold Regions Science and Technology*, **64**(2), 81–86, ISSN 0165-232X (doi:
756 <https://doi.org/10.1016/j.coldregions.2010.06.005>), international Snow Science Workshop 2009 Davos
- 757 Grenfell TC, Doherty SJ, Clarke AD and Warren SG (2011) Light absorption from particulate impurities
758 in snow and ice determined by spectrophotometric analysis of filters. *Appl. Opt.*, **50**(14), 2037–2048 (doi:
759 [10.1364/AO.50.002037](https://doi.org/10.1364/AO.50.002037))
- 760 Hagenmuller P, Matzl M, Chambon G and Schneebeli M (2016) Sensitivity of snow density and specific surface area
761 measured by microtomography to different image processing algorithms. *The Cryosphere*, **10**(3), 1039–1054 (doi:
762 [10.5194/tc-10-1039-2016](https://doi.org/10.5194/tc-10-1039-2016))
- 763 Haskell RC, Svaasand LO, Tsay TT, Feng TC, McAdams MS and Tromberg BJ (1994) Boundary conditions for the
764 diffusion equation in radiative transfer. *J. Opt. Soc. Am. A*, **11**(10), 2727–2741 (doi: [10.1364/JOSAA.11.002727](https://doi.org/10.1364/JOSAA.11.002727))
- 765 Henderson GR, Peings Y, Furtado JC and Kushner PJ (2018) Snow–atmosphere coupling in the northern hemisphere.
766 *Nature Climate Change*, **8**(11), 954–963 (doi: [10.1038/s41558-018-0295-6](https://doi.org/10.1038/s41558-018-0295-6))
- 767 Henley C (2020) Snow lidar monte-carlo simulator. Available at <https://github.com/co24401/SnowLiDARMonteCarlo>
- 768 Johansson J, Folestad S, Josefson M, Sparén A, Abrahamsson C, Andersson-Engels S and Svanberg S (2002) Time-
769 resolved nir/vis spectroscopy for analysis of solids: Pharmaceutical tablets. *Applied Spectroscopy*, **56**(6), 725–731
770 (doi: [10.1366/000370202760077676](https://doi.org/10.1366/000370202760077676))
- 771 Kienle A and Patterson MS (1997) Improved solutions of the steady-state and the time-resolved diffusion
772 equations for reflectance from a semi-infinite turbid medium. *J. Opt. Soc. Am. A*, **14**(1), 246–254 (doi:
773 [10.1364/JOSAA.14.000246](https://doi.org/10.1364/JOSAA.14.000246))
- 774 Kinar NJ and Pomeroy JW (2015) Measurement of the physical properties of the snowpack. *Reviews of Geophysics*,
775 **53**(2), 481–544 (doi: <https://doi.org/10.1002/2015RG000481>)
- 776 King F, Kelly R and Fletcher CG (2023) New opportunities for low-cost lidar-derived snow depth estimates from a
777 consumer drone-mounted smartphone. *Cold Regions Science and Technology*, **207**, 103757, ISSN 0165-232X (doi:
778 <https://doi.org/10.1016/j.coldregions.2022.103757>)
- 779 Kokhanovsky AA and Zege EP (2004) Scattering optics of snow. *Appl. Opt.*, **43**(7), 1589–1602 (doi:
780 [10.1364/AO.43.001589](https://doi.org/10.1364/AO.43.001589))
- 781 Konugolu Venkata Sekar S, Lanka P, Farina A, Dalla Mora A, Andersson-Engels S, Taroni P and Pifferi A (2019)
782 Broadband time domain diffuse optical reflectance spectroscopy: A review of systems, methods, and applications.
783 *Applied Sciences*, **9**(24), ISSN 2076-3417 (doi: [10.3390/app9245465](https://doi.org/10.3390/app9245465))
- 784 Lazarcik J, Dibb JE, Adolph AC, Amante JM, Wake CP, Scheuer E, Mineau MM and Albert MR (2017) Major
785 fraction of black carbon is flushed from the melting new hampshire snowpack nearly as quickly as soluble impurities.
786 *Journal of Geophysical Research: Atmospheres*, **122**(1), 537–553 (doi: <https://doi.org/10.1002/2016JD025351>)
- 787 Li C, Grobmyer SR, Massol N, Liang X, Zhang Q, Chen L, Fajardo LL and Jiang H (2008) Noninvasive in vivo
788 tomographic optical imaging of cellular morphology in the breast: Possible convergence of microscopic pathology
789 and macroscopic radiology. *Medical Physics*, **35**(6Part1), 2493–2501
- 790 Libois Q, Picard G, France JL, Arnaud L, Dumont M, Carmagnola CM and King MD (2013) Influence of grain shape
791 on light penetration in snow. *The Cryosphere*, **7**(6), 1803–1818 (doi: [10.5194/tc-7-1803-2013](https://doi.org/10.5194/tc-7-1803-2013))

- 792 Libois Q, Lévesque-Desrosiers F, Lambert-Girard S, Thibault S and Domine F (2019) Optical porosimetry of weakly
793 absorbing porous materials. *Opt. Express*, **27**(16), 22983–22993 (doi: 10.1364/OE.27.022983)
- 794 Liou KN, Takano Y, He C, Yang P, Leung LR, Gu Y and Lee WL (2014) Stochastic parameterization for light
795 absorption by internally mixed bc/dust in snow grains for application to climate models. *Journal of Geophysical*
796 *Research: Atmospheres*, **119**(12), 7616–7632 (doi: <https://doi.org/10.1002/2014JD021665>)
- 797 Malinka AV (2014) Light scattering in porous materials: Geometrical optics and stereological approach. *Journal of*
798 *Quantitative Spectroscopy and Radiative Transfer*, **141**, 14–23 (doi: <https://doi.org/10.1016/j.jqsrt.2014.02.022>)
- 799 McCullagh P (2019) *Generalized linear models*. Routledge
- 800 Nicolaï BM, Defraeye T, De Ketelaere B, Herremans E, Hertog ML, Saeys W, Torricelli A, Vandendriessche T and
801 Verboven P (2014) Nondestructive measurement of fruit and vegetable quality. *Annual Review of Food Science*
802 *and Technology*, **5**(1), 285–312 (doi: 10.1146/annurev-food-030713-092410), pMID: 24387604
- 803 Nienow PW and Campbell F (2011) Stratigraphy of snowpacks. In VP Singh, P Singh and UK Haritashya (eds.),
804 *Encyclopedia of Snow, Ice and Glaciers*, 1081–1084, Springer Netherlands, Dordrecht
- 805 Nolin A and Dozier J (2000) A hyperspectral method for remotely sensing the grain size of snow. *Remote sensing of*
806 *Environment*, **74**(2), 207–216
- 807 Okawa S and Hoshi Y (2023) A review of image reconstruction algorithms for diffuse optical tomography. *Applied*
808 *Sciences*, **13**(8), ISSN 2076-3417 (doi: 10.3390/app13085016)
- 809 Painter TH, Deems JS, Belnap J, Hamlet AF, Landry CC and Udall B (2010) Response of colorado river runoff
810 to dust radiative forcing in snow. *Proceedings of the National Academy of Sciences*, **107**(40), 17125–17130 (doi:
811 10.1073/pnas.0913139107)
- 812 Painter TH, Bryant AC and Skiles SM (2012) Radiative forcing by light absorbing impurities in snow from modis
813 surface reflectance data. *Geophysical Research Letters*, **39**(17) (doi: <https://doi.org/10.1029/2012GL052457>)
- 814 Quarto G, Spinelli L, Pifferi A, Torricelli A, Cubeddu R, Abbate F, Balestreri N, Menna S, Cassano E and Taroni
815 P (2014) Estimate of tissue composition in malignant and benign breast lesions by time-domain optical mammo-
816 graphy. *Biomed. Opt. Express*, **5**(10), 3684–3698 (doi: 10.1364/BOE.5.003684)
- 817 Robledano A, Picard G, Dumont M, Flin F, Arnaud L and Libois Q (2023) Unraveling the optical shape of snow.
818 *Nature Communications*, **14**(1), 3955 (doi: 10.1038/s41467-023-39671-3)
- 819 Satat G (2019) *All photons imaging : time-resolved computational imaging through scattering for vehicles and medical*
820 *applications with probabilistic and data-driven algorithms*. Ph.D. thesis, Massachusetts Institute of Technology,
821 Cambridge, MA
- 822 Schwarz JP, Gao RS, Fahey DW, Thomson DS, Watts LA, Wilson JC, Reeves JM, Darbeheshti M, Baumgardner
823 DG, Kok GL, Chung SH, Schulz M, Hendricks J, Lauer A, Kärcher B, Slowik JG, Rosenlof KH, Thompson TL,
824 Langford AO, Loewenstein M and Aikin KC (2006) Single-particle measurements of midlatitude black carbon
825 and light-scattering aerosols from the boundary layer to the lower stratosphere. *Journal of Geophysical Research:*
826 *Atmospheres*, **111**(D16) (doi: <https://doi.org/10.1029/2006JD007076>)
- 827 Sevick E, Chance B, Leigh J, Nioka S and Maris M (1991) Quantitation of time- and frequency-resolved optical
828 spectra for the determination of tissue oxygenation. *Analytical Biochemistry*, **195**(2), 330–351, ISSN 0003-2697
829 (doi: [https://doi.org/10.1016/0003-2697\(91\)90339-U](https://doi.org/10.1016/0003-2697(91)90339-U))

- 830 Skiles S, Flanner M, Cook J, Dumont M and Painter T (2018) Radiative forcing by light-absorbing particles in snow.
831 *Nature Clim. Change*, **8**(11), 964–971
- 832 Smith B, Studinger M, Sutterley T, Fair Z and Neumann T (2023) Understanding biases in icesat-2 data due to
833 subsurface scattering using airborne topographic mapper waveform data. *The Cryosphere Discussions [preprint]*,
834 1–29 (doi: 10.5194/tc-2023-147), in review
- 835 Smith BE, Gardner A, Schneider A and Flanner M (2018) Modeling biases in laser-altimetry measure-
836 ments caused by scattering of green light in snow. *Remote Sensing of Environment*, **215**, 398–410 (doi:
837 <https://doi.org/10.1016/j.rse.2018.06.012>)
- 838 Studinger M, Smith BE, Kurtz N, Petty A, Sutterley T and Tilling R (2024) Estimating differential penetration of
839 green (532 nm) laser light over sea ice with nasa’s airborne topographic mapper: observations and models. *The*
840 *Cryosphere*, **18**(5), 2625–2652 (doi: 10.5194/tc-18-2625-2024)
- 841 Várnai T and Cahalan RF (2007) Potential for airborne offbeam lidar measurements of snow and sea ice thickness.
842 *Journal of Geophysical Research: Oceans*, **112**(C12) (doi: <https://doi.org/10.1029/2007JC004091>)
- 843 Warren SG (2013) Can black carbon in snow be detected by remote sensing? *Journal of Geophysical Research:*
844 *Atmospheres*, **118**(2), 779–786 (doi: <https://doi.org/10.1029/2012JD018476>)
- 845 Warren SG (2019) Optical properties of ice and snow. *Philosophical Transactions of the Royal Society A: Mathemat-*
846 *ical, Physical and Engineering Sciences*, **377**(2146), 20180161 (doi: 10.1098/rsta.2018.0161)
- 847 Warren SG and Brandt RE (2008) Optical constants of ice from the ultraviolet to the microwave: A revised compi-
848 lation. *Journal of Geophysical Research*, **113**(D14)
- 849 Welch AJ and van Gemert MJ (1995) *Optical-thermal response of laser-irradiated tissue*. Springer, New York
- 850 Wiscombe WJ and Warren SG (1980a) A model for the spectral albedo of snow. i: Pure snow. *Journal of Atmospheric*
851 *Sciences*, **37**, 2712–2733
- 852 Wiscombe WJ and Warren SG (1980b) A model for the spectral albedo of snow. ii: Snow containing atmospheric
853 aerosols. *Journal of Atmospheric Sciences*, **37**(12), 2735–2745
- 854 Zappa F, Tisa S, Tosi A and Cova S (2007) Principles and features of single-photon avalanche diode arrays. *Sensors*
855 *and Actuators A: Physical*, **140**(1), 103–112, ISSN 0924-4247 (doi: <https://doi.org/10.1016/j.sna.2007.06.021>)
- 856 Zege E, Katsev I, Malinka A, Prikhach A, Heygster G and Wiebe H (2011) Algorithm for retrieval of the effective
857 snow grain size and pollution amount from satellite measurements. *Remote Sensing of Environment*, **115**(10),
858 2674–2685, ISSN 0034-4257 (doi: <https://doi.org/10.1016/j.rse.2011.06.001>)